electronics

MDPI

Article

Detection of Faulty Energizations in High Voltage Direct Current Power Cables by Analyzing Leakage Currents

Kumar Mahtani [1,*], Ricardo Granizo [2], José M. Guerrero [3] and Carlos A. Platero [1]

[1] Department of Electrical Engineering, Escuela Técnica Superior de Ingenieros Industriales, Universidad Politécnica de Madrid, 28006 Madrid, Spain; carlosantonio.platero@upm.es
[2] Department of Electrical Engineering, Escuela Técnica Superior de Ingeniería y Diseño Industrial, Universidad Politécnica de Madrid, 28012 Madrid, Spain; ricardo.granizo@upm.es
[3] Department of Electrical Engineering, Escuela de Ingeniería de Bilbao, Universidad del País Vasco, 48013 Bilbao, Spain; josemanuel.guerrerog@ehu.eus
* Correspondence: kumar.mahtani@upm.es

Abstract: The use of multi-terminal high voltage direct current (HVDC) power transmission systems is being adopted in many new links between different generation and consumption areas due to their high efficiency. In these systems, cable energization must be performed at the rated voltage. Healthy energizations at the rated voltage result in large inrush currents, especially in long cables, primarily due to ground capacitance. State-of-the-art protection functions struggle to distinguish between transients caused by switching and those associated with ground faults, leading to potential unwanted tripping of the protection systems. To prevent this, tripping is usually blocked during the energization transient, which delays fault detection and clearing. This paper presents a novel method for prompt discrimination between healthy and faulty energizations. The proposed method outperforms conventional protection functions as this discrimination allows for earlier and more reliable tripping, thus avoiding extensive damage to the cable and the converter due to trip blocking. The method is based on the transient analysis of the current in the cable shields, therefore, another technical advantage is that high voltage-insulated measuring devices are not required. Two distinct tripping criteria are proposed: one attending to the change in current polarity, and the other to the change in current derivative sign. Extensive computer simulations and laboratory tests confirmed the correct operation in both cases.

Keywords: cable energization; cable shielding; electrical fault detection; fault currents; ground faults; HVDC transmission; inrush current; leakage currents; power system faults; power system protection; power system transients; power transmission lines

Citation: Mahtani, K.; Granizo, R.; Guerrero, J.M.; Platero, C.A. Detection of Faulty Energizations in High Voltage Direct Current Power Cables by Analyzing Leakage Currents. *Electronics* **2024**, *13*, 4120. https://doi.org/10.3390/electronics13204120

Academic Editor: François Auger

Received: 5 August 2024
Revised: 9 October 2024
Accepted: 17 October 2024
Published: 19 October 2024

1. Introduction

The continuous increase in worldwide electrical power demand necessitates the construction of new and robust power transmission systems over long distances from generation plants to loads. The expansion of the electrical network also calls for the development of innovative techniques for energy transmission and power line protection. Traditionally, power has been transmitted using high voltage alternating current (HVAC) lines. However, high voltage direct current (HVDC) transmission systems are increasingly being adopted for new high-power, long-distance transmission projects [1,2]. Advancements in converter technology, such as the development of voltage-source converters (VSCs) [3], have enhanced the practicality of HVDC systems by enabling more compact and efficient designs.

HVDC systems offer a highly favorable solution for power transmission, with operating voltages ranging from 1 kV up to ±800 kV [4]. They are commonly used between converters, providing several advantages [5,6] including suitability for long-distance transmissions, asynchronous interconnection between converters, avoidance of reactive power compensation, and reduced environmental impact. One of the main benefits of HVDC

systems lies in the reduction in line losses, as only heat losses and power converter commutation losses are relevant. In contrast to HVAC systems, HVDC avoids inefficiencies such as reactive current components, skin and proximity effects, and induced currents in cable armature and sheaths. Furthermore, HVDC allows for precise power flow control and modulation capabilities, making it particularly useful for integrating renewable energy sources such as wind and solar power, into the grid, within the context of the energy transition. Despite these advantages, HVC systems present some drawbacks. The converters used in HVDC transmission introduce harmonics that can become problematic [7], and in the event of faults, the current exhibits a sharp gradient, reaching high values, thus complicating fault detection and protective relaying [8].

A significant advantage of HVDC technology over HVAC is its ability to transmit power over long distances without the limitations posed by capacitive charging currents in AC systems. In HVAC transmission, particularly in submarine or underground cables, capacitive charging currents increase with cable length, reducing the amount of active power that can be transmitted. For long distances, HVAC becomes impractical due to excessive losses and the requirement for reactive power compensation. In contrast, HVDC systems do not suffer from these limitations, allowing for much longer transmission distances with lower power losses, making HVDC particularly suitable for long-distance, high-capacity applications.

The distance at which HVDC becomes cost-competitive with HVAC systems ranges from 50 to 100 km for submarine and underground cables, and from 600 to 800 km for overhead lines [2,4]. This break-even point is achieved when the savings from reduced transmission losses outweigh the higher infrastructure costs of HVDC systems. Indeed, in terms of initial capital investment, HVDC systems are generally more expensive than their HVAC counterparts. This higher cost is primarily due to the HVDC substations [9], which require high voltage power converters such as line commutated converters (LCCs) or VSCs. Additionally, if DC circuit breakers are used, which must induce artificial current zero-crossings for circuit interruption, the cost of switchgears is further increased. A general cost breakdown of HVDC and HVAC systems including the location of the break-even point is shown in Figure 1.

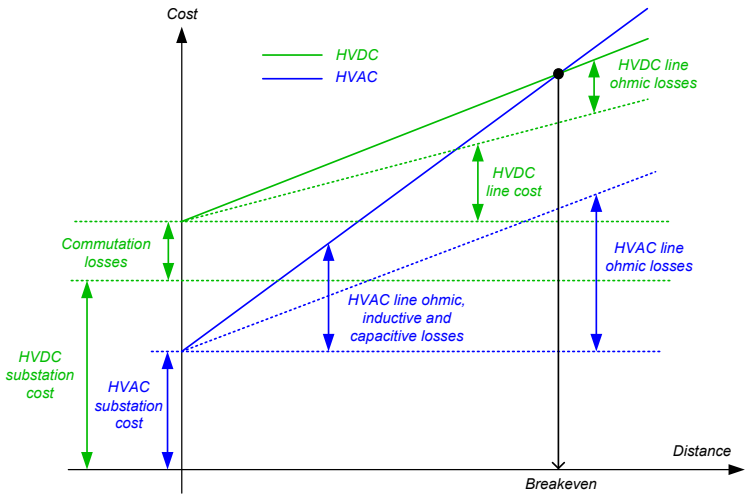

Figure 1. Comparison between HVDC and HVAC in terms of cost with respect to distance.

Multi-terminal HVDC networks, schematically represented in Figure 2, are the natural evolution of HVDC power transmission systems beyond traditional point-to point configurations. While energization in point-to-point HVDC transmission systems is typically performed at reduced voltage, in multi-terminal HVDC systems, new cables must be energized at the rated voltage to ensure seamless integration with the already energized network [10]. Consequently, the control strategy for starting up HVDC stations as well as the sequence for system energization must be carefully planned and executed. Proper

energization ensures the safe and reliable operation of HVDC systems, minimizing the risk of equipment damage, reducing downtime, and enhancing the overall efficiency of power transmission.

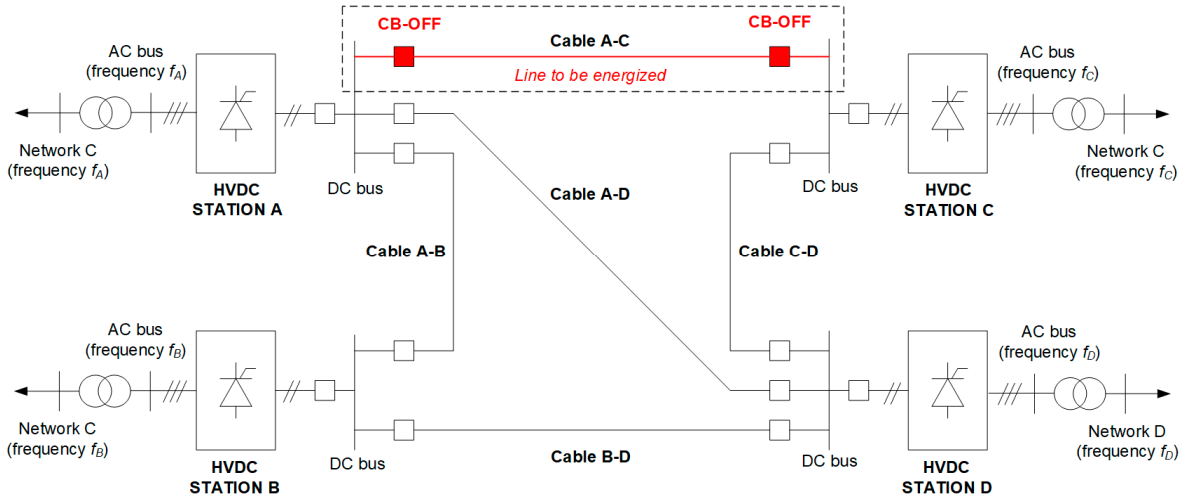

Figure 2. Simplified diagram of a multi-terminal HVDC network.

During energization [11,12], the voltage level rises rapidly as the HVDC link's capacitor charges to the rated voltage. Once the bus is charged, energization results in an instantaneous inrush of high current, accompanied by a temporary voltage dip that attenuates over time, harmonic injection, and dynamic overvoltages, which may lead to system instability. These effects are particularly pronounced in long-distance cables. Such phenomena can potentially interfere with the correct operation of protection systems.

Faulty energizations can occur when HVDC cables have a pre-existing ground fault. Although less frequent than in overhead lines, ground faults in HVDC cables are a significant concern because they are often permanent [13]. The primary causes of ground faults in HVDC cables include insulation deterioration due to aging, digging or anchoring (particularly in submarine cables), and improper installation. When a cable with a ground fault is energized [14–17], a large overcurrent is also generated, the magnitude of which depends on system grounding and fault resistance. If this fault current is not properly detected and interrupted, both the cable and the converters can be damaged. For instance, the high grid current contribution to the fault can flow through the freewheeling diodes, potentially affecting the converter valve.

Discerning whether a transient is caused by the energization of a healthy cable or a ground fault remains a challenging task, crucial for avoiding spurious protection triggering. This paper presents a novel method for distinguishing between healthy and faulty energizations by analyzing shield currents during cable energization [18]. The shield current measurements are conducted using only low voltage (LV)-insulated equipment, allowing for the diagnosis and protection of HVDC cables without the need for high voltage (HV)-insulated equipment.

The rest of this paper is structured as follows. Section 2 reviews the previous methods currently in use. Section 3 describes the operating principles of the proposed method. Sections 4 and 5 present various computer simulations and experimental laboratory tests, respectively, to doubly validate the method. Finally, Section 6 highlights the main ideas and contributions of the paper.

2. Technical Background

2.1. Protection of Multi-Terminal HVDC Systems

In multi-terminal HVDC cable networks, it is essential to quickly remove faulty cables from service. Protection relays for HVDC power systems need to operate faster than those

used in HVAC systems due to the rapid development of high fault currents [19]. The most effective fault clearing strategy implies opening the breakers located at both cable ends [20].

The need for reliable fault detection and protection methods in HVDC systems is related to the semiconductors used in converter stations, which have limited overcurrent capacity, often requiring fault-blocking [21–25]. If multiple converters are switched-off, the HVDC system may collapse, compromising the stability of the HVDC system, and potentially leading to a blackout [26–28].

Various protection techniques can be employed in HVDC systems [13,29–32]. These techniques can be categorized into single-ended and double-ended protection schemes, as illustrated in Figure 3. Single-ended schemes are based on local monitoring of the DC current and voltage waveforms, while double-ended schemes are based on the real-time communication between the ends of the protection zone.

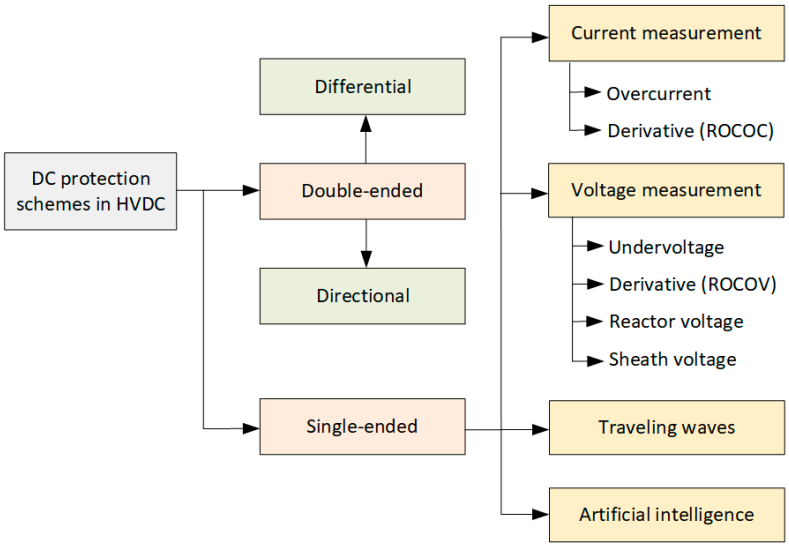

Figure 3. Main DC fault detection techniques in HVDC systems.

Double-ended schemes are inherently selective but less suitable for primary protection in HVDC lines due to the limited operational speed imposed by the communication channel and the reduced reliability related to contingencies affecting the same. Therefore, single-ended schemes will be addressed in this work. The following subsections will delve into key aspects of single-ended DC-side protection techniques for HVDC systems [13,29–32].

2.2. Overcurrent and Undervoltage Protections

In conventional overcurrent and undervoltage protection algorithms, DC current or voltage, respectively, are locally monitored and compared with a preset threshold. Additionally, directionality can be achieved by monitoring the polarity. Although these conventional protection methods are characterized by their fast operation, their main drawback is their lack of selectivity, which can lead to the unnecessary tripping of adjacent lines. This can result in broader system outages than intended.

Furthermore, the settings of these methods to detect [33] or even locate [34] faults in overground and underground HVDC line sections are based on theoretical fault current analysis and rely on the currents or voltage measurements at the converter stations connected to the lines. These theoretical models do not account for the dynamic conditions encountered in HVDC systems, especially during energizations, where large inrush currents may be mistaken for fault conditions. This could potentially lead to false tripping or to delayed fault clearing if the tripping is blocked during the maneuver.

Furthermore, accurately setting the protection time characteristic necessitates precise modeling of the power system dynamics responsible for fault current contributions.

Achieving this level of precision is challenging. Therefore, these functions are generally employed as backup protection in HVDC systems.

2.3. Current and Voltage Derivative-Based Protections

In current-based derivative schemes, the rate of change of current, denoted as di/dt (ROCOC), is compared to a preset threshold [35]. This method exploits the fact that ROCOC increases significantly during faults.

The main advantage of the current-based approach is the ability to identify faults well before reaching their peak fault value. This method operates notably faster than overcurrent and undervoltage functions. Furthermore, directional selectivity can be added if the current polarity is analyzed.

However, high and ultra-high arc resistance may impair the effectiveness of this protection method, as transient currents in such cases can resemble those produced by switching operations. Therefore, ROCOC protections are unsuitable to distinguish between normal switching operations such as energizations and fault conditions. This reason often leads to the use of trip blocking to prevent false triggering. Another drawback of this method is that selectivity issues can persist, especially for high-resistance faults, as the ROCOC for an external fault may induce triggering. Furthermore, large sampling frequencies are required to accurately calculate the ROCOC, as their accuracy is influenced by the feeder length, and the selectivity can be reduced for lines with lower impedance. The method is also vulnerable to noisy environments and can be susceptible to misoperations due to inappropriate measurement sampling.

One notable development in current-based derivative schemes is based on the behavior of the converter filter capacitor during a fault. When a fault occurs, the capacitor discharges and supplies current to the fault, prior to the diode freewheeling and grid current feeding stages. The current dynamics depends on the fault location and the cable inductance. If the ratio of the capacitor voltage drop to di/dt is less than the cable inductance, L_{cable}, a trip is triggered [27]. This technique remains unaffected by the fault resistance, which makes the method perform effectively even with high fault resistances, since the rate of change is predominantly influenced by the fault location. However, a drawback of this method is the rapid exponential decay of the rate of change, which implies that even minor delays in measurements can lead to inaccuracies. To eliminate the influence of fault location, further developments consider the correlation between the ROCOC of the DC link capacitor and the line ROCOC. Although these converter filter capacitor-based methods obtain good results under steady-state conditions, unwanted trips can occur during maneuver transients such as energizations.

In the case of voltage-based derivative schemes, the rate of change of voltage, dV/dt (ROCOV), is involved [36]. This method leverages the fact that the ROCOV sharply increases at the onset of a fault compared to normal operating conditions.

ROCOV protections share most of the advantages and disadvantages mentioned for ROCOC protections, allowing for almost instantaneous fault detection. Most importantly, as ROCOV tends to decrease substantially when the distance between the fault location and the measurement point increases, it can allow discrimination between internal and external faults, but its selectivity is also compromised for faults with high fault resistance. Neither ROCOV-based methods can distinguish between voltage drops caused by transients associated with switching operations, such as energizations, and those deriving from fault conditions.

ROCOC and ROCOV protections usually need to be integrated with other criterion to develop selective and reliable algorithms. Moreover, they require HV-insulated equipment to provide the measurements, as the operativity of these methods relies on the current or voltage measurements at the output of the converter stations.

2.4. Reactor Voltage-Based Protections

This approach utilizes the voltage across the limiting inductor as a fault indicator when its value exceeds the predefined threshold. ROCOV can be employed within the same inductor for faster operational speed [36–38]. In this regard, by comparing the voltages on either side of the current-limiting reactors, one can discern whether the fault is at the bus or line side, ensuring selectivity.

This approach presents the advantage of leveraging the smoothing reactors beyond their main purpose of limiting the increase in fault currents by serving as boundary markers to divide the system into separate protection zones. This enables discrimination between the internal and external faults as the main benefit. However, like conventional ROCOV-based methods, no protective criteria based on reactor voltage reported in the literature have addressed the differentiation between healthy and faulty line connections to the network. Another significant drawback is that without any other auxiliary protection, the scheme's reliability can be compromised in the presence of high-resistance faults [39]. The fault resistance as well as the transmission line length can deeply affect the accuracy of the protection scheme. Furthermore, the DC reactors installed at the positive and negative poles must have exactly equal values, otherwise asymmetric pole inductor configurations may fail to detect asymmetrical faults such as ground faults. In any case, HV-insulated equipment is required to obtain the voltage measurements at both sides of the reactors.

2.5. Sheath Voltage-Based Protections

Under normal operating conditions, the transient voltage in the grounded cable sheath is typically zero. In the event of a fault, the transient voltage rises, and the fault current flows through the sheath. The amplitude of this transient voltage and its polarity can be utilized to detect the faulty cable segment and identify the affected pole. Specifically, the cable segment and pole with the highest sheath voltage are indicated as faulty. Additionally, analyzing the polarity of the transient voltage can help distinguish between faults and capacitor imbalances. In cases of capacitor imbalance, the transient voltage will exhibit the opposite polarity compared to that of a faulty condition [40,41].

Sheath voltage-based protection offers a relatively simple and prompt method for detecting ground faults in HVDC lines, requiring only LV-insulated equipment consisting of sheath voltage metering devices installed at the end of each cable. However, signal attenuation and delays in the transient voltage can create challenges in accurately detecting and locating faults, particularly when they occur far from the measuring point. Additionally, transient events such as switching operations or energizations produce transient voltage signatures similar to those of certain faults, capacitor imbalances, or other disturbances, potentially leading to false fault detections if the polarity is not properly analyzed. This discrimination issue remains a challenge for sheath voltage-based methods, which has not been addressed in previous works.

2.6. Other Methods

Other single-ended protection techniques include those that detect traveling waves (TWs) generated during faults and those that utilize artificial intelligence (AI). TW-based protection methods employ mathematical transforms, such as Fourier or Wavelet transforms, to analyze the wave's frequency components and distinguish between fault conditions and normal operation. In contrast, AI-based methods replicate human decision-making through computational models. While both TW and AI-based protection can offer high reliability, they come with high computational complexity. TW-based methods encounter challenges in mathematically modeling the TWs, detecting the wave-head, and identifying faults near the measuring point. Additionally, they require high sampling rates. AI-based methods, though potentially accurate, robust and fast, involve complex and time-consuming algorithm construction stages, such as the training phase for artificial neural networks, and necessitate high-quality initial datasets. Most of these techniques also

require HV current or voltage measurements as inputs, and none have specifically focused on the detection of faulty energizations in HVDC lines.

2.7. Problem Statement

In point-to-point HVDC lines, the energization currents under normal conditions are typically not large enough to trigger the incorrect operation of protection relays, as these energizations are performed at reduced voltages. However, in multi-terminal HVDC networks, where energizations are conducted at the rated voltage, high inrush currents can potentially lead to the erroneous tripping of protection systems. This occurs because the previously discussed protection techniques fail to adequately distinguish between transients caused by switching operations on a healthy HVDC cable and those resulting from a ground fault. To prevent spurious triggering due to mismatches caused by energization inrush currents, it is common practice to introduce a time-delay parameter in the protection settings. While this approach reduces false tripping, it also delays the clearing of ground faults until the trip blocking delay, potentially causing damage to the cable and converter. This problem, which has not been addressed in the state-of-the-art described in the previous sections, is illustrated in Figure 4.

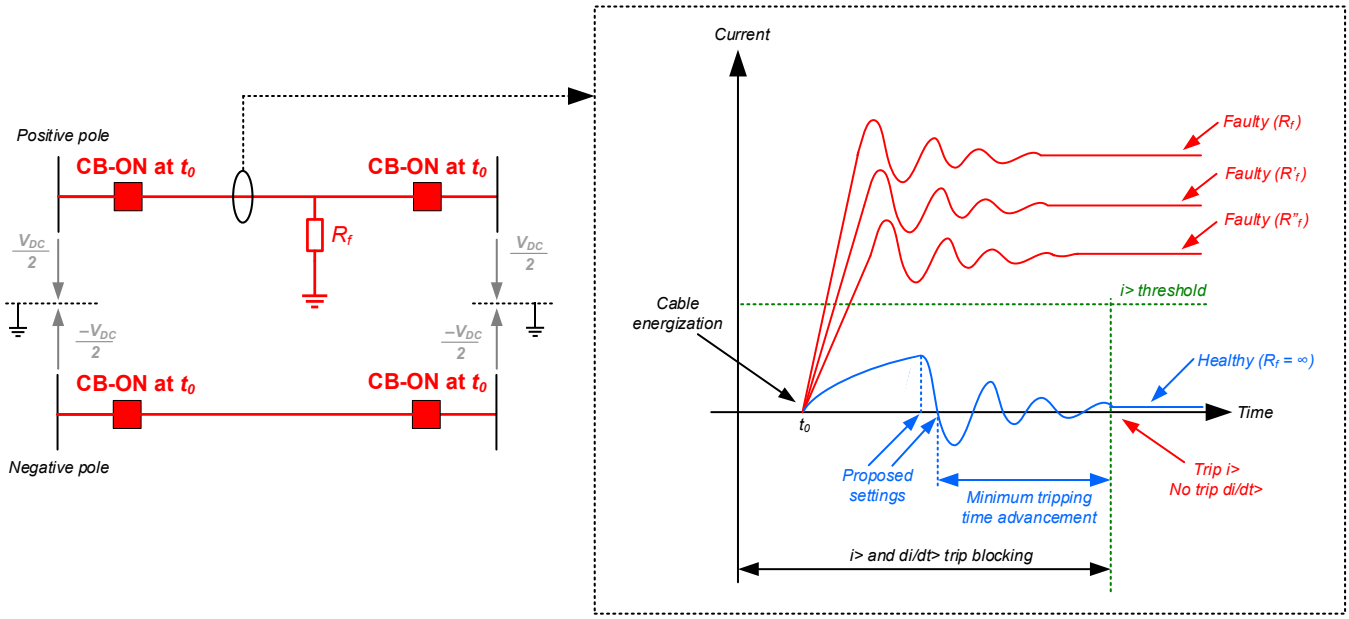

Figure 4. Bipolar HVDC line from a multi-terminal HVDC network energized at $t = t_0$ with a ground fault present on the positive pole: schematic representation and current waveforms.

In Figure 4, the energization of a bipolar HVDC line at time $t = t_0$ is depicted. This HVDC line is part of the multi-terminal HVDC network shown in Figure 2. The energization is conducted at the rated voltage of the line, denoted as V_{DC}. A ground fault is present on the positive pole during energization, with fault resistance $R_f < R'_f < R''_f$ (underdamped response without zero-crossing is assumed in all faulty cases, see Section 3.1). For instance, when overcurrent (i>) or current derivative (di/dt>)-based protection functions are considered, their inability to distinguish between switching transients and those associated with ground faults necessitates the use of a time-delay parameter to avoid false tripping. During this delay, tripping is blocked, leaving the system unprotected. The trip blocking time is typically set to the duration in which the current, during a healthy energization (with $R_f = \infty$), is expected to reach the steady state. After this period, i> may trip if the current exceeds the threshold, although di/dt> may not trip, as the DC steady state has already been reached. It is important to note that this approach inherently delays fault clearing at least until after the trip blocking time, during which the high fault current may cause significant damage.

To avoid trip blocking and enable earlier fault detection and clearing, it is necessary to reliably distinguish between healthy and faulty HVDC cable energizations. The method proposed in this work addresses this problem by analyzing characteristic transient current features to determine whether the energization occurs under healthy or faulty conditions. As illustrated in Figure 4, the criteria proposed in this work allow for a maximum tripping time to be set that is significantly shorter than the conventional trip blocking time (proposed setting), advancing fault detection and clearing, and notably avoiding fault persistence in time (minimum tripping time saving).

Additionally, a key constraint to the stated problem is the requirement of using LV-insulated equipment instead of HV-insulated devices. Unlike most existing protection techniques, which rely on HV-insulated measuring devices, the proposed method should operate based on current measurements from the cable shield, instead of currents or voltages on the line or at the converter stations as most of the state-of-the-art aforementioned methods, except for Section 2.5. Previous works have successfully utilized shield current measurements to detect ground faults in HVDC cables within multi-terminal networks [42,43], demonstrating notable cost efficiency and technical simplicity.

3. Principles of the Proposed Method

As developed in the previous section, in multi-terminal HVDC power systems, cable energization must be performed at the rated voltage since it must connect to an already energized busbar. Energizing long cables results in large inrush currents, even under normal conditions. These inrush currents should not trigger the cable protection system; otherwise, the line cannot be energized. However, if a ground fault occurs during energization, the protection system should trip as quickly as possible. As healthy energization currents can exhibit high values similar to fault currents, the challenge of differentiating healthy and faulty cable energization must necessarily be addressed.

This paper introduces a method to differentiate between healthy and faulty HVDC cable energization based on the circulation of shield currents. Current measurements are taken at the cable shields, requiring only LV-insulated devices. Ground faults are detected by analyzing the features of the transient oscillation of these currents [44,45] and comparing them with specific thresholds. In the following subsections, the theoretical and operational principles of the proposed method are presented.

3.1. Theoretical Principles of the Proposed Method

In Figure 5, a bipolar HVDC configuration is represented, with positive and negative polarity cables and a shared grounded neutral point. DC voltage sources and a load resistor are represented in a generalized form. In this example, a DC link with three cable sections is considered, with a ground return assumed. The cable shield is grounded at both ends, and in these shield-to-ground connections, current measurement sensors (A) are installed. These sensors were included at the DC source end of each cable shield. Figure 5 illustrates the current distribution in the shields with a ground fault in either pole of the HVDC line at steady state. The currents circulating upstream and downstream are represented in red and blue, respectively.

In the event of an internal ground fault in the cable, the fault current circulating through the shield will have a high value. For a ground fault in the positive DC cable shown in Figure 5a, the positive shield current sensor will detect the large DC component with a positive sign. Conversely, if the negative line is healthy, no significant currents will be measured in the negative shield current sensor. Figure 5b shows the negative cable fault case in a similar manner.

In this regard, it should be noted that while the number and location of grounding points—typically in the form of distributed grounding systems in HVDC networks—affect the magnitude of the shield current, this current will necessarily flow through the cable shields, attenuated by fault resistance, due to the proximity to the fault, provided that the shield is grounded at both ends.

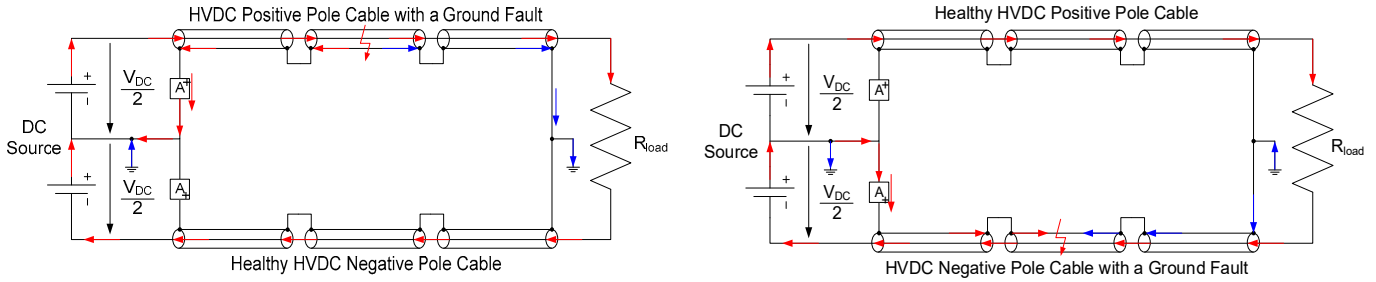

Figure 5. Ground faults in a simple HVDC transmission cable. (**a**) Current flow for a ground fault in the second section of positive pole. (**b**) Current flow for a ground fault in the second section of the negative pole.

The proposed protective topology, by placing the sensors in the closed shield ground circuit, ensures proper selectivity, as only faults within the protection zone, specifically those that cause current to flow through the cable shield, typically resulting from pole-to-ground faults, will trigger the operation. In the context of multi-terminal HVDC networks, this protection ensures that only the affected line will trip, leaving the other lines in the system unaffected, minimizing system disruption and isolating the fault in an efficient manner. The proposed protection method should be activated during energizations while other protective schemes are disabled or blocked, ensuring proper coordination through time selectivity.

The equivalent circuit of the HVDC line under healthy conditions, modeled with lumped parameters in a π-section and assuming symmetrical conditions for illustrative purposes, is depicted in Figure 6. This circuit considers the cable resistance (R_C) and inductance (L_C), the shield resistance (R_S) and inductance (L_S), the cable-shield mutual inductance (M_{CS}), and the cable-to-shield shunt capacitance (C_{CS}) and resistance (R_{CS}), while neglecting the shield-to-ground capacitance with respect to the solid grounding connection. The shield current measured at the shield-to-ground connection (I_{shield}) is represented for the positive pole as an example. Upon energization by stepwise connection to the voltage source with initially uncharged shunt capacitors, these behave like short-circuits presenting minimal resistance to current flow. As the capacitors charge, the voltage across their terminals increases, resulting in a decrease in current. This phenomenon is due to the accumulation of charge within the capacitors, which generates an opposing electric field that resists the inflow of additional charge. Therefore, during normal energization, the shield current, due to inrush currents, exhibits an initial overshoot followed by damped oscillations around the zero-value DC component, as the shield currents equal zero in the steady-state condition.

The surge of shield current that occurs when the line is energized can be significantly high and depends on the energization voltage, which corresponds to the rated voltage in the case of multi-terminal HVDC line energization and the load connected upon energization. Additionally, the surge of current is affected by the cable capacitance, with longer HVDC transmission lines exhibiting greater shield current flow during energization due to the additive effect of length on capacitance. Furthermore, temperature, humidity, and other environmental factors, given their influence on electrical properties, also impact the surge of shield current. At the converter station side, upstream of the equivalent circuit shown in Figure 6, the following factors also influence the current spike:

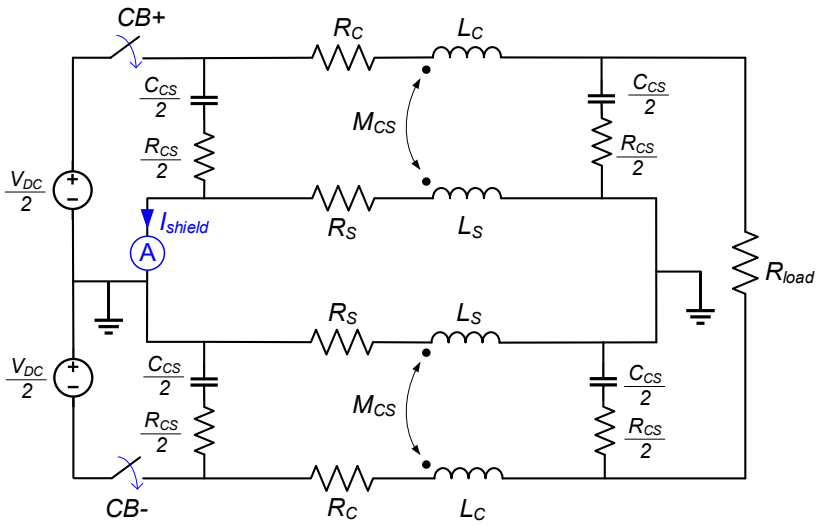

Figure 6. Circuit model of the HVDC line considering lumped parameters.

- Converter station capacitance including filter banks and smoothing capacitors;
- Inductive elements including transformers and reactors;
- Converter impedance;
- Switching time and circuit breaker characteristics;
- AC system impedance.

The behavior of $I_{shield}(t)$ after the voltage step in $V_{DC}(t)$ applied at $t_0 = 0$ depends on the nature of the system's poles, which are determined by the system's characteristic equation derived from the governing differential equations. In the high-order response for $I_{shield}(t)$ in the circuit depicted in Figure 6, the contribution of non-dominant poles can be neglected, and the system can be approximated by a second-order system that will determine, according to the damping ratio (ζ), whether $I_{shield}(t)$ exhibits an underdamped sinusoidal response or a spike followed by exponential decay to zero.

For an underdamped system ($\zeta < 1$), which is the general case in long transmission lines under healthy conditions and the one that will be considered in this work, a damped sinusoidal response is developed, with both sine and cosine components in the most general form, as in Equation (1), where ω_n is the natural frequency of the system and A and B are constant values that can be determined by applying the initial conditions. Equation (1) can be simplified into Equation (2) if the $I_{shield}(0) = 0$ condition is known, while if $I_{shield} \to 0$ is known at the steady-state condition, then $K = 0$. The first zero-crossing of $I_{shield}(t)$, occurring at $t = t_c$, is computed in Equation (3), while the first zero-crossing of the time derivative of $I_{shield}(t)$, occurring at $t = t_d$, is computed in Equation (4).

$$I_{shield}(t) = e^{-\zeta\omega_n t}\left[A\cos\left(\omega_n\sqrt{1-\zeta^2}t\right) + B\sin\left(\omega_n\sqrt{1-\zeta^2}t\right)\right] + K \quad (1)$$

$$I_{shield}(t) = Be^{-\zeta\omega_n t}\sin\left(\omega_n\sqrt{1-\zeta^2}t\right) \quad (2)$$

$$I_{shield}(t_c) = 0 \;\to\; t_c = \frac{\pi}{\omega_n\sqrt{1-\zeta^2}} \quad (3)$$

$$\frac{dI_{shield}}{dt}(t_d) = 0 \;\to\; t_d = \frac{\arctan\frac{\sqrt{1-\zeta^2}}{\zeta}}{\omega_n\sqrt{1-\zeta^2}} \quad (4)$$

The equivalent circuit of the HVDC line under faulty conditions as well as with lumped parameters, broken down into two π-sections (upstream and downstream of the ground fault), is depicted in Figure 7. A general ground fault in a relative location x in the positive cable with a fault resistance R_f is represented ($x = 0$ at the converter end and $x = 1$

at the load end of the HVDC line). In order to study the behavior of I_{shield} in this case, a similar procedure can be conducted, noting that the shunt capacitance cannot be generally neglected during energization for all R_f values.

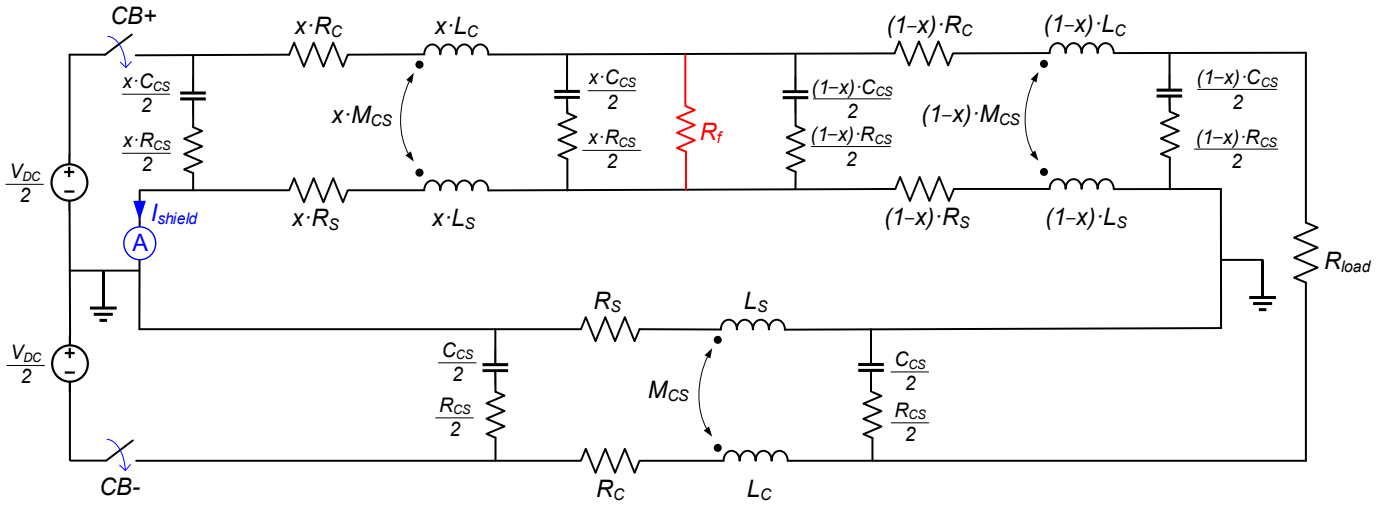

Figure 7. Circuit model of the HVDC line considering lumped parameters with a ground fault in the positive pole.

Adding a ground fault with a fault resistance R_f in the equivalent circuit, as shown in Figure 7, corresponds to an additional shunt resistance between the faulty cable and ground, in parallel with the effect of the distributed shunt capacitance over the cable length. The presence of the ground fault reduces the ground impedance, thus increasing the damping ratio ($\zeta_h < \zeta_f$) depending on the value of R_f and the fault location, making the system more overdamped. Ground faults closer to the measuring end and with lower R_f values contribute to greater damping. As a result, the oscillations will decay more quickly and the response will approach the steady state more rapidly. For a certain fault location, the system will have a greater damping effect for lower R_f values, and for a sufficiently low value of R_f, the system may be overdamped rather than underdamped under faulty conditions if ζ exceeds 1 when the ground fault is included.

If the system is underdamped under faulty conditions ($\zeta_h < \zeta_f < 1$), upon energization, an initial overshoot to the peak value is exhibited in I_{shield}, depending on the fault location and resistance, followed by damped oscillations while settling to the constant DC value in the steady state, which is reflected in Equation (5). Equation (5) can be particularized for I_{shield} (0) = 0 and $I_{shield} \rightarrow K$ (the measured shield current is positive, $K > 0$, at the steady-state condition, as a result of the ground fault), resulting in Equation (6). Solving the zero-crossing condition for $I_{shield}(t)$, as stated in Equation (7), requires numerical methods or iterative techniques as the equation combines exponential and trigonometric forms in t. If a solution exists, the system will exhibit a zero-crossing (underdamped response with zero-crossing). Otherwise, in most cases, this equation will not exhibit any solution, implying that no zero-crossing will occur, as after the initial overshoot, the response will develop as damped oscillations around K above the origin, without polarity variation (underdamped response without zero-crossing). Particularly, if the most extreme theoretical approach is adopted, assuming that the exponential term is close to 1 for low t values, therefore neglecting the damping effect, and that at least one zero-crossing is produced, it can be demonstrated that the first zero-crossing time under faulty conditions ($t_{c,f}$) is larger than the one under healthy conditions ($t_{c,h}$), as per Equation (8).

$$I_{shield}(t) = e^{-\zeta\omega_n t}\left[C\cos\left(\omega_n\sqrt{1-\zeta^2}t\right) + D\sin\left(\omega_n\sqrt{1-\zeta^2}t\right)\right] + K \quad (5)$$

$$I_{shield}(t) = e^{-\zeta\omega_n t}\left[-K\cos\left(\omega_n\sqrt{1-\zeta^2}t\right) + D\sin\left(\omega_n\sqrt{1-\zeta^2}t\right)\right] + K \tag{6}$$

$$I_{shield}(t_c) = 0 \;\rightarrow\; t_c \approx \frac{2\pi + \arctan\left(-\frac{D}{K}\right) \pm \arccos\frac{K}{\sqrt{K^2+D^2}}}{\omega_n\sqrt{1-\zeta^2}} \tag{7}$$

$$t_{c,h} = \frac{\pi}{\omega_n\sqrt{1-\zeta_h{}^2}} < t_{c,f} \approx \frac{2\pi + \arctan\left(-\frac{D}{K}\right) \pm \arccos\frac{K}{\sqrt{K^2+D^2}}}{\omega_n\sqrt{1-\zeta_f{}^2}} \tag{8}$$

In order to find the first derivative sign change of $I_{shield}(t)$, the expression provided in Equation (6) will be differentiated and its first zero-crossing will be computed, as per Equation (9). Similarly, it can be demonstrated that the time for the first derivative sign change under faulty conditions ($t_{d,f}$) occurs later than the one under healthy conditions ($t_{d,h}$), as per Equation (10).

$$\frac{dI_{shield}}{dt}(t_d) = 0 \;\rightarrow\; t_d = \frac{\frac{\pi}{2} + \arctan\frac{K\sqrt{1-\zeta^2}-\zeta D}{D\sqrt{1-\zeta^2}+\zeta K}}{\omega_n\sqrt{1-\zeta^2}} \tag{9}$$

$$t_{d,h} = \frac{\arctan\frac{\sqrt{1-\zeta_h{}^2}}{\zeta_h}}{\omega_n\sqrt{1-\zeta_h{}^2}} < t_{d,f} = \frac{\frac{\pi}{2} + \arctan\frac{K\sqrt{1-\zeta_f{}^2}-\zeta_f D}{D\sqrt{1-\zeta_f{}^2}+\zeta_f K}}{\omega_n\sqrt{1-\zeta_f{}^2}} \tag{10}$$

If the system is overdamped under faulty conditions ($\zeta > 1$), it is worth noting that a spike followed by an exponential decay to steady state develops without oscillations, as in Equation (11). This equation can then be simplified into Equation (12) if the initial condition I_{shield} (0) = 0, the dominant pole condition, and the steady-state condition $I_{shield} \rightarrow K$ are applied under faulty conditions, and the time constant (τ) is defined. Ground faults closer to the measuring end and with lower R_f values contribute to lower time constants, resulting in faster dynamic evolution to the steady state. As derived from Equation (12), no zero-crossing is present after t = 0 as $I_{shield}(t)$ follows an exponential growth evolution toward K (horizontal asymptote). Furthermore, the time derivative of $I_{shield}(t)$ expressed in Equation (13) follows an exponential decay toward zero (horizontal asymptote). Therefore, neither zero-crossing nor derivative sign change are produced if the faulty system presents an overdamped response.

$$I_{shield}(t) = C_1 \cdot e^{s_1 \cdot t} + C_2 \cdot e^{s_2 \cdot t} \tag{11}$$

$$I_{shield}(t) = K \cdot (1 - e^{-\frac{t}{\tau}}) \tag{12}$$

$$\frac{dI_{shield}}{dt}(t) = \frac{K}{\tau} \cdot e^{-\frac{t}{\tau}} \tag{13}$$

Regardless of the transient response type, the steady-state DC current value after a faulty energization, corresponding to K in the previous analytical developments, can be obtained from the equivalent circuit in the steady-state conditions depicted in Figure 8. The expression for $K = I_{shield}(\infty)$ as a function of the fault resistance and location (R_f and x) is given in Equation (14). As expected, from Equation (14), it is evident that K is greater for lower x values (ground faults closer to the converter end, in which shield-to-ground current is measured) and for lower R_f values, with the solid ground fault (R_f = 0) being the most severe case.

$$K = (1-x) \cdot \frac{V_{DC}}{2} \cdot \frac{1 - \frac{x \cdot R_c}{(1-x)\cdot R_c + R_{load} + R_c}}{x \cdot R_c \cdot \left[1 + \frac{R_s \cdot x \cdot (1-x) + R_f}{(1-x)\cdot R_c + R_{load} + R_c}\right] + R_s \cdot x \cdot (1-x) + R_f} \tag{14}$$

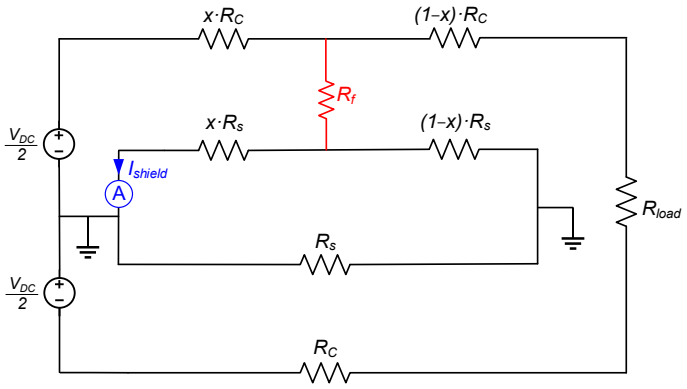

Figure 8. Circuit model of the HVDC line considering lumped parameters with a ground fault in the positive pole for the steady-state condition.

Finally, it should be noted that the amplitude of the initial oscillations measured at the shield grounding connection in a healthy energization is influenced by several key factors related to the system's electrical characteristics, notably the distribution of the system impedances, which ultimately affects the effective voltage applied to the distributed cable-to-shield capacitance, among the factors previously mentioned. For faulty energizations, characteristic features, such as the peak current in the case of underdamped response, also depend on the ground fault resistance and location, in addition to the electrical characteristics of the circuit. Therefore, any protection based solely on the current magnitude is subject to mismatches between healthy and faulty energizations.

3.2. Operational Principles of the Proposed Method

The distinction between the shield current waveform for normal switching-on and a ground fault can be leveraged to develop a protection criterion to reduce unwanted trips during cable energization. Thus, ground fault detection is achieved by analyzing the shield current, $I_{shield}(t)$, and using a predefined criterion adjusted for a specific threshold time after energization. In the following, an energization performed at $t = t_0$ will be considered, and therefore the protection setting criteria will be referred to as time lapses after energization ($\Delta t = t - t_0$).

One possible threshold setting (Δt_c) is based on the first zero-crossing of the shield current waveform under healthy energization, as per Equation (15). If, at this time, the shield current in any energization is present with the same initial polarity above a certain current threshold not far from zero (ε_c), this implies that DC current is circulating due to a ground fault, and the relay should trip the corresponding breaker, as in Equation (16). Analogously, the polarity of this current would be the opposite in the case of the shield current measured in the shield-to-ground connection of the negative pole, as in Equation (17), allowing for faulty pole identification.

$$\Delta t_c = t_{c,h} - t_0 = \left[I^{-1}_{shield}(0) \right]_h \tag{15}$$

$$[I_{shield}(\Delta t_c)]_+ > |\varepsilon_c| > 0 \rightarrow Fault\ in\ (+) \rightarrow Trip \tag{16}$$

$$[I_{shield}(\Delta t_c)]_- < -|\varepsilon_c| < 0 \rightarrow Fault\ in\ (-) \rightarrow Trip \tag{17}$$

During a healthy energization, the shield currents will exhibit intense oscillations due to inrush currents, but this is not the case in a faulty energization, as described above. Therefore, an alternative threshold setting (Δt_d) is based on the first zero-crossing of the shield current derivative (i.e., derivative sign change) under healthy energization, as per Equation (18). If, at this time, the shield current derivative in any energization exhibits the same initial sign above a certain current threshold not far from zero (ε_d), this implies that DC current is circulating due to a ground fault, and the relay should trip the corresponding breaker. Based on the sign of this derivative, faults in the positive cable, as in Equation (19),

and in the negative cable, as in Equation (20), can be detected, as the derivative sign of the shield current measured in the shield-to-ground connection of the negative pole will be the opposite. This criterion also allows for faulty pole identification and notably faster tripping in the event of a faulty energization compared to the zero-crossing criterion.

$$\Delta t_d = t_{d,h} - t_0 = \left[\left(\frac{dI_{shield}}{dt} \right)^{-1} (0) \right]_h \tag{18}$$

$$\left[\frac{dI_{shield}}{dt} (\Delta t_d) \right]_+ > |\varepsilon_d| > 0 \rightarrow Fault\ in\ (+) \rightarrow Trip \tag{19}$$

$$\left[\frac{dI_{shield}}{dt} (\Delta t_d) \right]_- < -|\varepsilon_d| < 0 \rightarrow Fault\ in\ (-) \rightarrow Trip \tag{20}$$

It should be noted that ε_c and ε_d represent safety factors to avoid spurious triggering and false tripping, which can cause slight deviations from zero in the current or its derivative. These safety margins depend on the HVDC line and its operating environment (e.g., noise levels, converter stations) and should be fine-tuned during protection commissioning. Furthermore, the sensitivity and selectivity of the proposed method are addressed in Section 3.3.

Both tripping criteria are illustrated in Figure 9, although they can be combined in order to enhance reliability. In any case, the characteristics of healthy energization should be known in order to perform protection setting. It is worth noting that, for the zero-crossing criterion, the time threshold (Δt_c) should be set at least after the completion of the first oscillation or semi-period in a healthy energization (i.e., at least for the Δt_c value complying with Equation (15)). Similarly, for the derivative sign change criterion, the time threshold (Δt_d) should be set at least after the attainment of the first current peak in a healthy energization (i.e., at least for the Δt_d value complying with Equation (18)). Nevertheless, a certain time delay can be applied in both cases for reliability purposes. Alternatively, trip blocking is also possible through this fault detection method, as if the shield current exhibits zero-crossings or both positive and negative slopes within the threshold time, this would indicate a healthy energization.

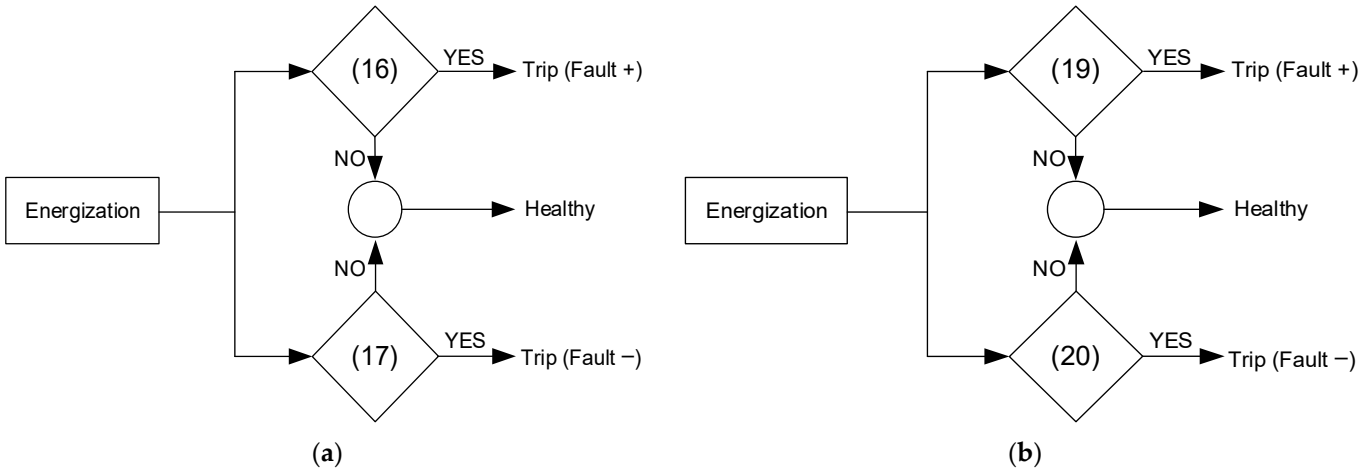

Figure 9. Summary of the tripping criteria. (**a**) Zero-crossing criterion. (**b**) Derivative sign change criterion.

Figure 10 summarizes the different faulty condition cases that have been addressed in this section according to the response of the faulty circuit to energization (underdamped responses with and without zero-crossing and overdamped response), and illustrates the practical application of the tripping criteria in all three cases. It should be noted that the characteristic transient response of the faulty circuit in Figure 7 depends on the RLC values

of the same that give rise to the characteristic constants, therefore, the response is expected to be different for each HVDC cable.

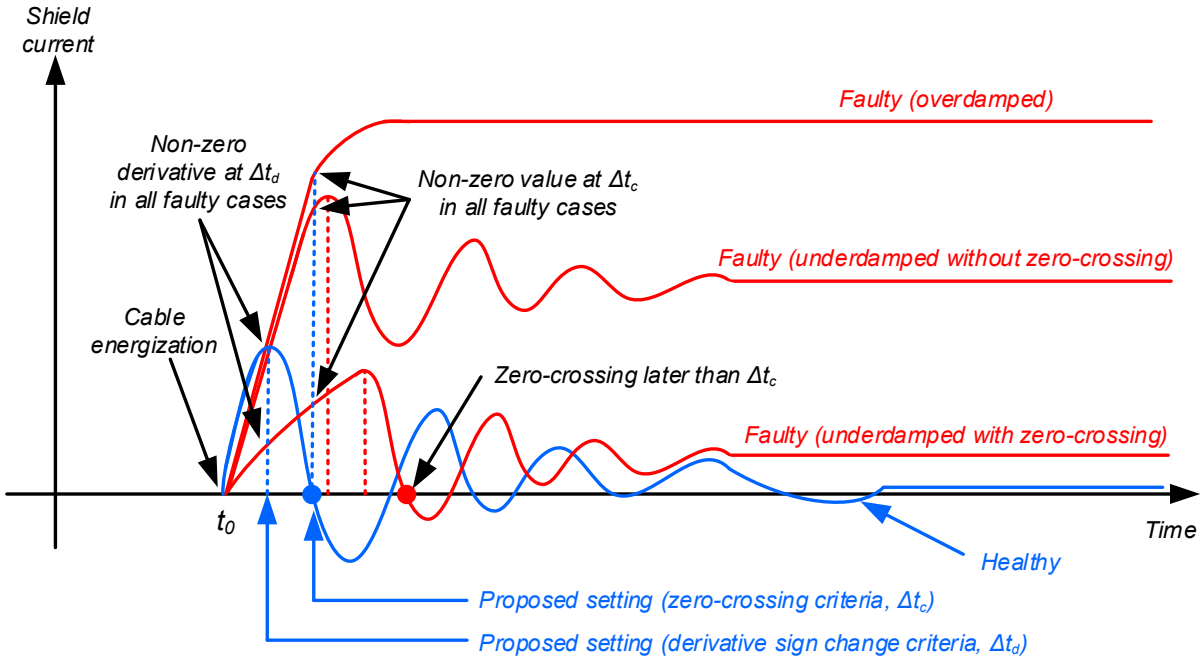

Figure 10. Graphical summary of the tripping setting and different faulty shield currents according to the characteristic response of the faulty circuit to energization (fault in the positive pole).

Although normal switching operations can cause step-type load changes causing step currents in both the bus and ground circuits, the transient currents in the ground circuit—mainly due to cable-to-shield ground capacitance—are much smaller than for ground faults. This method leverages the predictable behavior of healthy energizations, where zero-crossings occur at expected intervals, ensuring that normal load changes do not trigger false fault indications. This discrimination even holds for high-resistance ground faults, as healthy switching maneuvers do not produce a steady-state DC component, unlike ground faults.

3.3. Selectivity and Sensitivity of the Proposed Method

Zone selectivity ensures that only internal pole-to-ground faults within the protected cables will trigger the protection system during energization. In fact, the shield currents are influenced by the inductive coupling or mutual inductance between the conductor and the shield, while all other coupling or circuit continuities with other systems are negligible. As a result, the proposed topology ensures that shield current sensors detect disturbances exclusively within the local protection zone: only faults within this zone will trigger the protection system. Faults occurring outside the protection zone will not induce current through the monitored cable shield, leaving the cable grounding circuit and the inductive coupling within the protected zone unaffected. Zone selectivity is a strict requirement in multi-terminal HVDC networks, where only the affected line should be isolated to prevent disruption to the rest of the system.

Time selectivity, on the other hand, refers to the coordination of protection timing with other relaying functions. The proposed function is designed to solely activate during energizations, as it operates within the time window corresponding to the first half-cycle of the shield current waveform. If no fault is detected within the time intervals (Δt_c or Δt_d), the protective function is deactivated, and conventional HVDC protective schemes should take the responsibility for detecting the fault.

According to the principles described in Sections 3.1 and 3.2, in any faulty energization, the shield current will necessarily exhibit a non-zero value at Δt_c, and a non-zero derivative

at Δt_d, regardless of the type of characteristic response. These unique electrical signatures form the basis of the operational principles to detect faulty energizations, inherently providing selectivity. However, several factors that could lead to false tripping should be considered for fine-tuning during protection commissioning:

1. Electromagnetic interference (EMI): Inductive coupling, capacitive coupling, or improper grounding with multiple earth references can induce low-frequency transient currents in the cable shield, potentially mimicking fault conditions and leading to false trips if the protection system is not properly set.
2. High-frequency oscillations: Converter operations, high-frequency external noise, or transient conditions in the network can trigger false fault detections if the protection system settings are inadequate. High-frequency random noise also falls under this category.
3. Measurement noise: External interference or sensor inaccuracies can introduce high-frequency noise spikes that exceed the threshold and cause a false trip. Particularly, the signal-to-noise characteristics of the current sensors used in any implementation of the method should be subjected to study.

Considering the possible presence of these false tripping factors, an initial healthy energization should be performed in any specific implementation of the method, in order to extract the required setting parameters. Each specific application of the method implies unique RLC cable parameters, resulting in different time constants and circuit responses to the step voltage (e.g., underdamped with or without zero-crossing, or overdamped) as well as particular environmental noise sources. Additionally, the value of R_f impacts the characteristic response of the faulty circuit, which may vary from that of the healthy circuit. Therefore, a detailed case-by-case analysis is required to fine-tune the protection system in each practical implementation.

An example of the analysis of false tripping factors and the fine-tuning process for protection setting is provided in Section 5.4, which also evaluates the selectivity and sensitivity of the proposed method in the practical case.

4. Computer Simulations

4.1. Simulation Model

To validate the premises described above, computer simulations were conducted using ATPDraw® software [46], version 5.9p4, a graphical, mouse-driven preprocessor to the Alternative Transients Program (ATP) version of the Electromagnetic Transients Programs (EMTP) on the MS-Windows® platform. This choice was based on the proven effectiveness in handling the intricacies of HVDC systems including detailed modeling of the cable characteristics, converter behaviors, and fault analysis.

Figure 11 illustrates the model used for the simulations. This model comprises three sections of a 220-kV DC link (SEC-1, SEC-2 and SEC-3), each section being 100 km long. The cable's cross-section configuration is shown in Figure 12. Table 1 presents the technical and dimensional features of the HVDC cable used in these simulations. The characteristic impedance of the cable was included in the model to account for reflections and interactions at the terminations. The HVDC converter was modeled as a 12-pulse thyristor bridge. A main DC circuit breaker was placed at the sending end of the HVDC cable. The closing of this circuit breaker allowed us to energize the HVDC line.

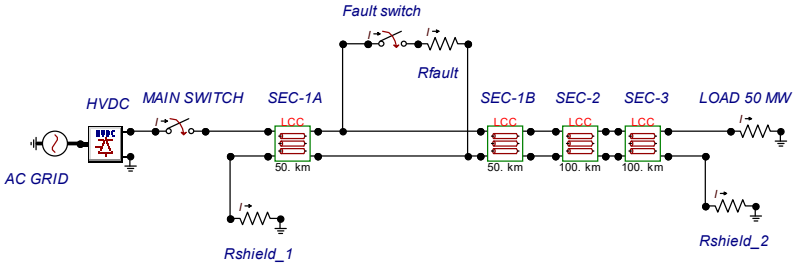

Figure 11. Simulation model overview.

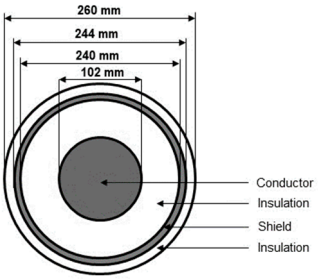

Figure 12. HVDC cable cross-section and main dimensions.

Table 1. Characteristics of the simulated HVDC cable.

Symbol	Magnitude	Value	Unit
ρ_{Al}	Aluminum resistivity	2.82×10^{-8}	Ω·m
ρ_{Al}	Copper resistivity	1.71×10^{-8}	Ω·m
ε_{cs}	Conductor-to-shield relative permeability	2.5	
ε_{se}	Shield-to-ground relative permeability	2.3	
l	Cable section length	100	km
$V_{n,DC}$	Rated continuous DC voltage	±320	kV
$V_{SIWL,DC+}$	Switching impulse withstand level (SIWL)	698	kV
$V_{SIWL,DC-}$	Subtractive SIWL	378	kV
$I_{n,DC}$	Rated continuous DC current	1638	A
θ_{max}	Maximum conductor temperature	70	°C
$R_{20°C}$	DC resistance at 20 °C	0.0072	Ω/km
$R_{70°C}$	DC resistance at	0.0087	Ω/km
$P(I_{n,DC})$	Losses at the rated current	23.3	W/m
C	Capacitance	0.28	µF/km
L	Conductor-to-shield inductance	0.127	mH/km
Z_0	Surge impedance	21.4	Ω
$I_{sc,c}$	Max. short-circuit current during 0.2 s	32	kA
$I_{sc,s}$	Max. short-circuit shield current during 0.2 s	16	kA

The time-domain simulations were performed with a fixed step size of 10^{-6} s to ensure accurate representation of rapid transient phenomena. The cable was modeled with Semlyen's frequency-dependent parameters, considering a frequency-dependent simple fitted model [47], accounting for the variations in cable impedance with changing frequencies encountered during the transient. The simulation boundary conditions regarding cable terminations were modeled as a voltage source to apply the rated DC voltage during energization on the sending end, and as an equivalent resistive load to emulate 50 MW power transmission on the receiving end. Regarding grounding boundary conditions, the shield terminals were grounded through grounding resistors ($R_{shield\_1} = R_{shield\_2} = 0.1\ \Omega$) at both side ends. The simulation's initial conditions implied cable voltage and currents set to zero during the pre-energization stage.

Healthy condition simulations as well as several faulty condition simulations corresponding to ground faults with different fault resistance values (R_{fault}) occurring at a

point located 50 km into the first section (between section SEC-1A and section SEC-1B in Figure 11) were conducted. The faults were simulated by initially closing the fault switch.

4.2. Healthy Energization Simulations

Once the simulation parameters were established, several healthy energization simulations were conducted. In Figure 13, the current evolution in the cable shield near the power source is displayed, measured at the shield-to-ground connection of the positive pole when the cable is energized under healthy conditions. Both no-load and 50 MW load condition energizations are presented. The energization was performed 100 ms after the simulation started for the no-load case, and 105 ms for the loaded case. The shield current waveforms exhibited underdamped responses, with initial oscillations with characteristic periods of approximately 30 ms, which were dampened to a zero-value DC component at steady-state conditions. The damping was greater for the loaded energization (58.10% attenuation) than for the unloaded energization (33.26% attenuation). The extinction of the energization current could clearly be observed at approximately 400 ms after the energization for the no-load case, and at approximately 300 ms for the loaded case. This oscillating characteristic and damping to zero are indicators of successful energization.

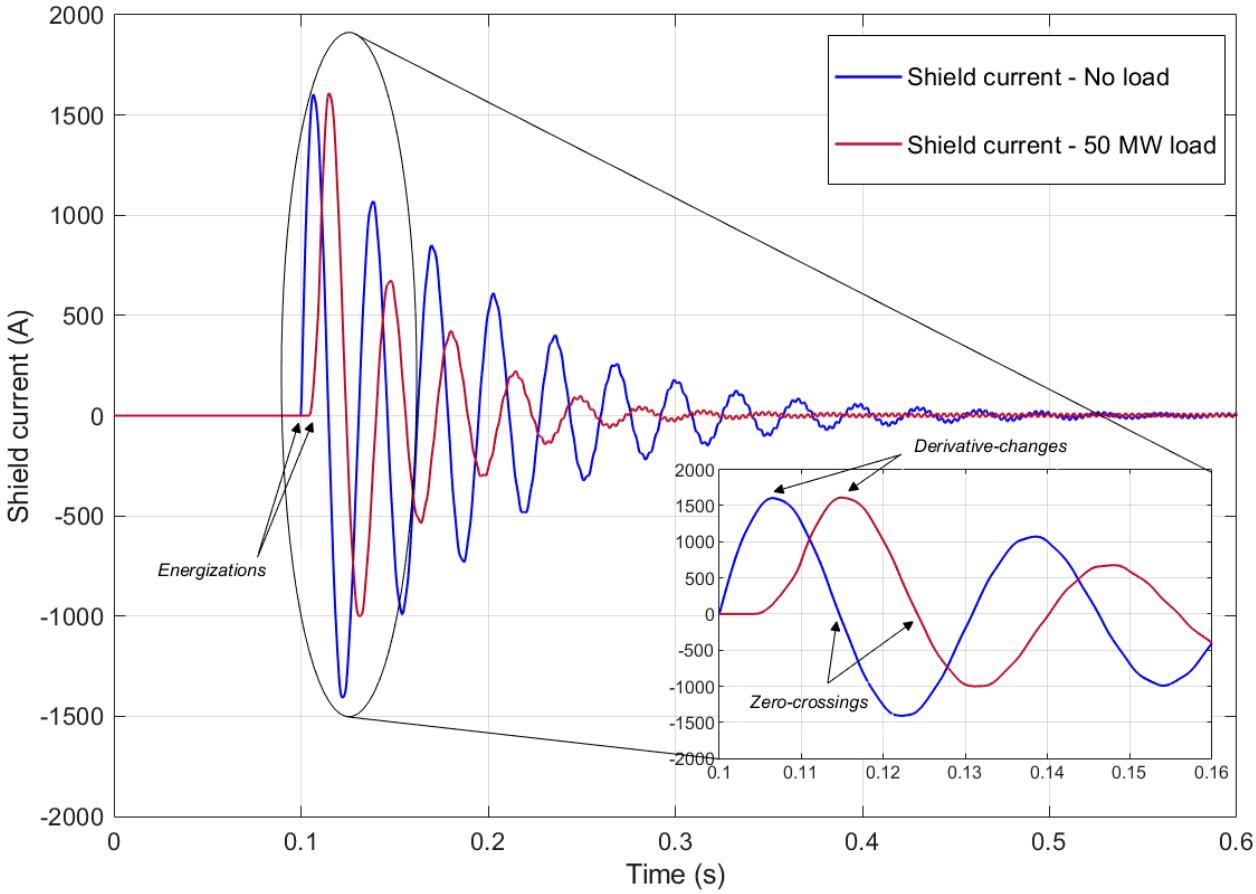

Figure 13. Simulation results. Shield currents for healthy energizations: no-load and 50 MW load cases.

In Figure 13, it can be observed that the first shield current zero-crossings occurred at 14.638 ms and 20.018 ms after energization for the no-load and 50 MW load cases, respectively. Differences in the zero-crossing times imply different Δt_c time threshold settings (Δt_c = 14.638 ms and Δt_c = 20.018 ms, respectively), in accordance with Equation (15). Additionally, in Figure 13, it can be observed that the derivative sign changes occurred at 6.691 and 10.067 ms after energization for the no-load and 50 MW load cases, respectively. Once again, different Δt_d time thresholds should be set (Δt_d = 6.691 ms and

Δt_d = 10.067 ms, respectively) in accordance with Equation (18). The derivative sign change criterion allowed for earlier fault detection than the zero-crossing criterion ($\Delta t_d < \Delta t_c$) in any of the cases. These findings are aligned with the principles described in Section 3 and will be employed for fault detection in the following.

4.3. Faulty Energization Simulations

In the event of a faulty energization, the shield current near the power source reaches higher values than in the healthy energization. Figures 14a and 14b illustrates the shield current at the power source end, measured at the shield-to-ground connection of the positive pole for unloaded and 50 MW loaded condition energizations, respectively. In both cases, the cable was assumed to have an internal ground fault 50 km from the power source in the positive pole (between section SEC-1A and section SEC-1B in Figure 11). The energization was performed 100 ms after the simulation started. Different fault resistance (R_f) values were considered for each load condition: 0.01, 1, 10, and 100 Ω.

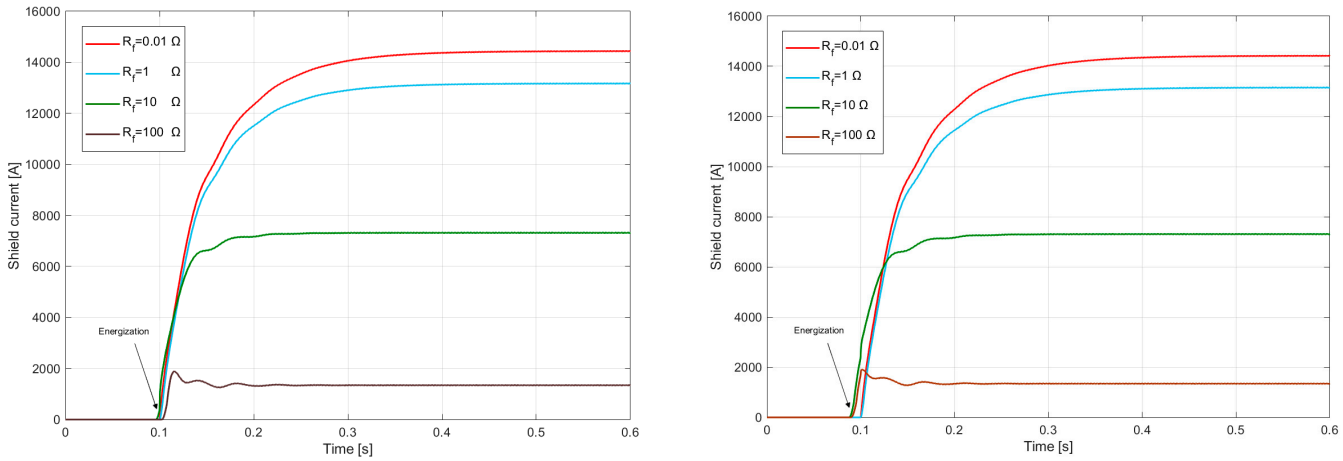

Figure 14. Simulation results. Shield currents for energizations with a ground fault at 50 km for different fault resistance values (R_f = 0.01, 1, 10 and 100 Ω): (**a**) no-load condition; (**b**) 50-MW load.

The results uphold the contribution of the ground fault to increasing the damping of the shield current measured in the transient stage after energization, with lower R_f values implying greater damping effect, eventually turning overdamped for the tested R_f values of 0.01, 1, and 10 Ω, as it can be seen in Figure 14. In this respect, the oscillations were negligible compared to the DC component for low R_f values but they started to be significant for higher R_f values, as it can be seen for R_f = 100 Ω. Furthermore, as expected, the steady state the DC component attained after the transient stage was greater for more severe faults (i.e., for lower R_f values).

The results showed that during the faulty energizations, the shield current only had a positive sign throughout the entire process and subsequent time. Analogously, this current remained negative throughout the process and subsequent time if the fault was performed in the negative pole. In all faulty cases, the shield current settled to a constant DC value with the corresponding polarity in the steady state. Thus, no zero-crossing was attained in the shield current waveform. Comparing Figures 14a and 14b, it was observed that the differences in shield current, measured at the shield-to-ground connection at the power source end, for loaded and unloaded conditions, were not significant. For example, 20 ms after energization, the shield currents attained 5.2, 4.8, 4.1 and 1.6 kA for fault resistances of 0.01, 1, 10, and 100 Ω, respectively. These values, significantly above zero, uphold the applicability of the zero-crossing criterion as per Equation (16). It can be derived that fault detection based on the zero-crossing criterion becomes more challenging for higher R_f values, as the current values approach the ones achieved under the healthy condition.

The results also showed that during the faulty energizations, the shield current derivative only had a positive sign throughout the entire process and subsequent time for tested R_f values of 0.01, 1 and 10 Ω, as these responses were assimilable to a second-order overdamped transient. This evidences the applicability of the derivative sign change criterion for faulty overdamped evolutions, although it becomes more challenging for higher R_f values such as R_f = 100 Ω, for which the response is underdamped and the first derivative sign change approaches the one achieved under the healthy condition.

The shield current waveforms for healthy and faulty energizations are presented in Figure 15 for the no-load case as an example, with a certain time difference for clarity purposes. The faulty energizations corresponded to the less severe and thus most challenging studied ground fault (R_f = 100 Ω). In this figure, the time threshold settings at their minimum operable values, according to the previously described healthy unloaded energizations, are indicated for both tripping criteria (Δt_c = 14.638 ms and Δt_d = 6.691 ms).

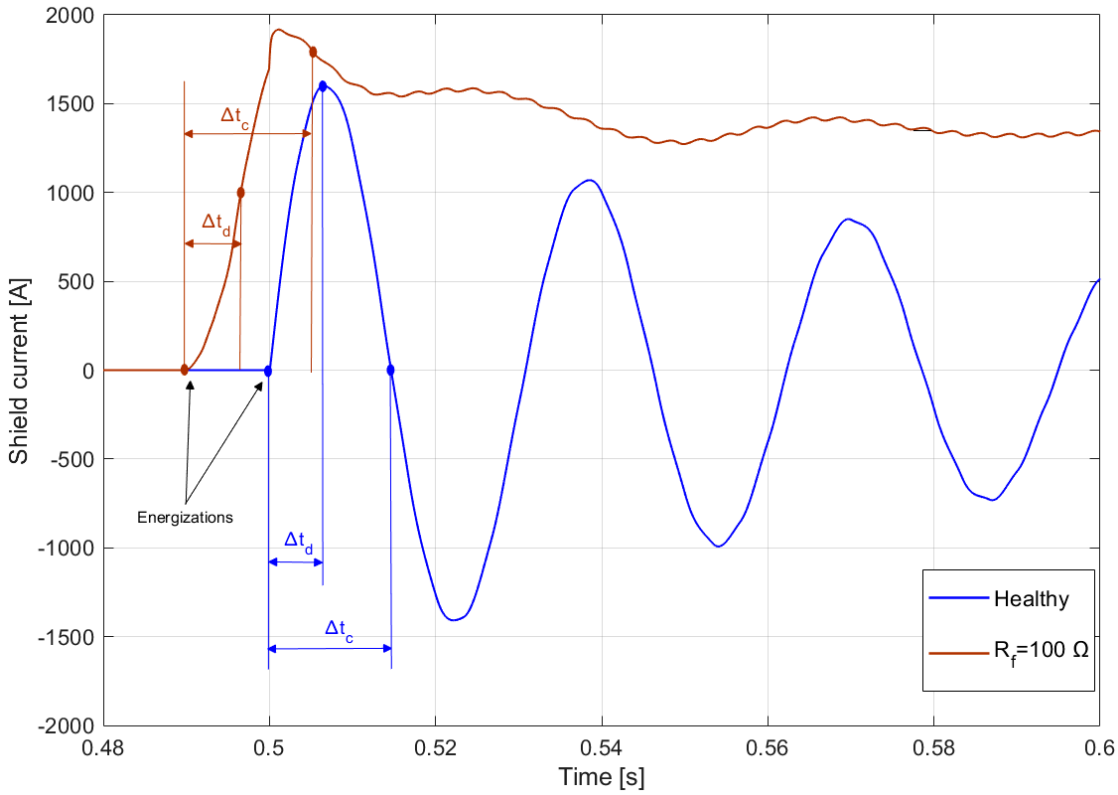

Figure 15. Simulation results. Shield currents: comparison between no-load healthy and faulty energizations. Ground fault at 50 km with R_f = 100 Ω.

In Figure 15, for the zero-crossing criterion, at the threshold time of Δt_c = 14.638 ms after energization, the current was zero for the healthy energization and 1.82 kA for a faulty energization (R_f = 100 Ω), complying with the criterion established in Equation (16). However, if the minimum time lapse under healthy conditions is known (14.638 ms in this case), a time delay could be operable. For example, for a setting of 15 ms after energization, if within this time the current has not yet exhibited a polarity change, the ground fault can be inferred. This criterion can even be easily applied for higher R_f values, as long as the faulty shield current is non-negligible.

Similarly, for the derivative sign change criterion, for the threshold time of Δt_d = 6.691 ms after energization, the derivative was zero for the healthy energization, while for the faulty energization, the shield current continued to grow with a clearly possible derivative, complying with the criterion established in Equation (19). Once again, if the minimum time lapse under healthy conditions is known (6.691 ms in this case), a time delay above this value could be operable. For example, for a setting of 7 ms after energization, if within

this time the current has not yet exhibited an extremum, the ground fault can be inferred. This criterion allows for faster tripping, but it should be managed carefully, as for higher R_f values, the extremums for faulty and healthy energization can be close in time (in this case, 10.991 ms under the faulty condition with respect to 6.691 ms under the healthy condition, which is still an operable difference).

The numerical application of the tripping criteria to the simulations results is presented in Table 2.

Table 2. Numeral application of the tripping criteria to the simulation results for a ground fault in the positive pole at 50 km, with settings of Δt_c = 14.638 ms and Δt_d = 6.691 ms.

R_f [Ω]	I_{shield} [kA] at Δt_c	(16) Verified	dI_{shield}/dt [kA/s] at Δt_d	(19) Verified
0.01	5.38	Yes	18.1	Yes
1	4.92		16.3	
10	4.88		12.2	
100	1.82		6.4	

It is worth noting that in the case of a loaded energization, the same logic would apply, with the threshold setting being performed according to the corresponding loaded healthy energization characteristic. For a ground fault in the negative pole, the results are analogous, but for negative polarity, Equations (17) (the current remains with a non-negligible negative value after Δt_c) and (20) (the current continues to decrease instead of attaining a local minimum within Δt_d) are applied. Furthermore, according to the shield grounding connection for which these conditions are satisfied (positive or negative), the faulty pole can be easily identified. However, it is clear that fault location cannot be determined by current amplitudes, as they are dampened by the fault distance and resistance.

From Figures 14 and 15, it can be derived that if ordinary derivative-based (di/dt) protection functions are applied during energization, the system would lack selectivity, failing to distinguish between healthy and faulty energizations, especially in the case of high fault resistance. Indeed, if the fault goes unnoticed by the di/dt function, the persistence of the final DC component through the cable shield can be dangerous or even destructive. Additionally, if commonly used overcurrent (i>) protection functions are applied during energization, the system would also fail to distinguish between current peaks in healthy and faulty energizations with high fault resistance. Nevertheless, alternatively, overcurrent protection could be applied after the zero-crossing time threshold, although the fault detection would be largely delayed with respect to the proposed criteria.

In conclusion, the simulation results validate the method for ground fault detection during energizations. The differences in the shield current or derivative values, with respect to the healthy energization characteristic, are adequate indicators to effectively determine whether an energization is healthy or faulty. The derivative criterion allows for faster fault detection than the zero-crossing criterion, although for high fault resistance faults, the latter setting is more suitable. A combination of both criteria would increase the reliability of the protection.

5. Experimental Tests

5.1. Experimental Setup

To verify the proposed method, numerous laboratory experimental tests were conducted. The schematic layout of the experimental setup is depicted in Figure 16. This setup included an AC power supply connected to an autotransformer capable of varying the voltage between 0 and 400 V, and a 400/100 V Δ-Y step-down transformer that isolated the experimental setup from the laboratory ground. Additionally, a three-phase LV circuit breaker was used as the energization switch. A full-wave rectifier consisting of six diodes, a C = 13 μF capacitor bank with an intermediate common grounded neutral point, and 300 m of coaxial cable (comprising three 100 m sections) were connected. The main characteristics

of each cable section were R = 1.8 Ω, L = 22 mH, and C = 4.9 nF. The shields had identical RLC values. At the end of the cable, a 100 Ω resistor emulated the load. The cable shields were grounded at both ends.

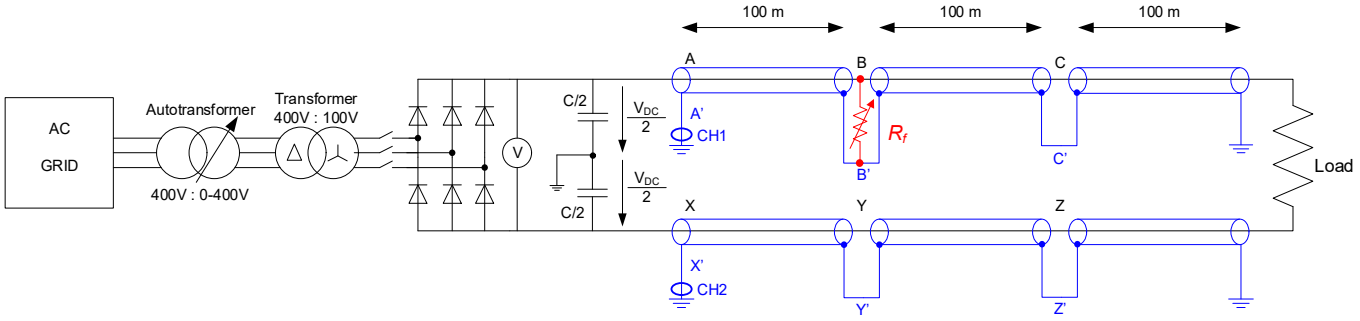

Figure 16. Schematic layout of the experimental setup. A ground fault in the positive cable at point B-B′ and a 100 Ω resistive load is represented.

The terminals of each 100 m cable section and their respective shields were accessible. Thus, in Figure 16, these terminals are represented as A, B, and C for the conductor at locations 0, 100, and 200 m from the rectifier side, respectively, and A′, B′, and C′ for the corresponding shield points, along the positive cable. Similarly, along the negative cable, terminals X, Y, and Z for the conductor and X′, Y′, and Z′ for the corresponding shield points were enabled at the same mentioned locations. This allowed for ground fault performance at these locations. A rheostat was used to emulate fault resistance, allowing short-circuiting of the cable or its respective shield within a range of 0 to 600 Ω. Particularly, for these experimental tests, fault resistance values of 0, 1, 10, and 100 Ω were used.

Regarding the measuring instrumentation, two current clamps were placed in the shield ground connection at the power source end in order to monitor the shield currents (CH1 for the positive cable shield and CH2 for the negative cable shield). These currents were recorded by an oscilloscope. A voltmeter was placed at the DC side terminals of the rectifier to control the voltage during the tests (50 V_{DC}). A caption of the experimental setup, indicating all the described elements, is shown in Figure 17.

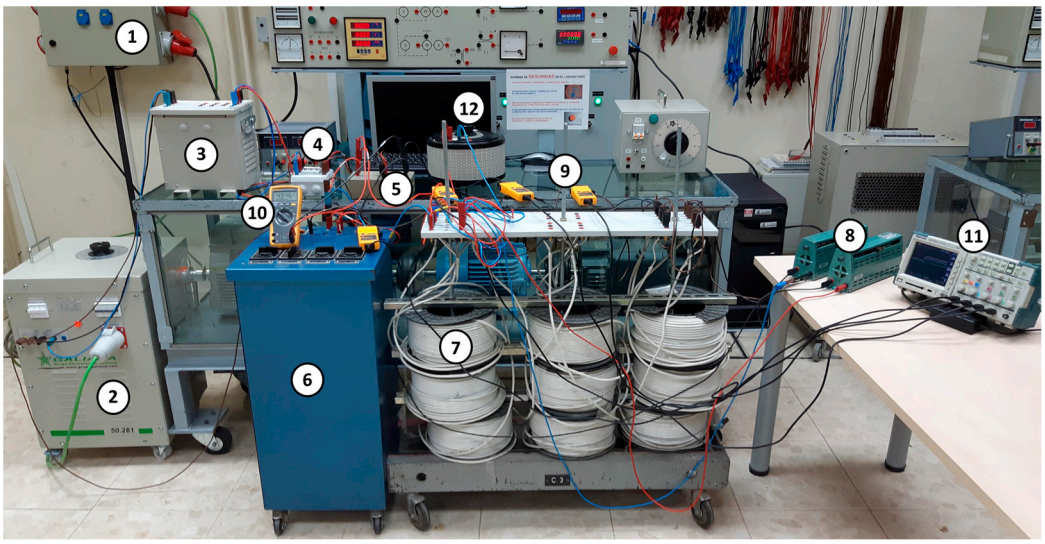

Figure 17. Experimental setup (1: AC power supply, 2: autotransformer, 3: step-down transformer, 4: energization switch, 5: three-phase rectifier bridge, 6: capacitor bank, 7: 300 m DC cable, 8: resistive load, 9: ammeter clamp, 10: voltmeter, 11: oscilloscope, 12: rheostat).

5.2. Healthy Energization Tests

Different healthy energization tests were conducted under a 100 Ω resistive load at 50 V_{DC}. Figure 18 shows the shield current evolution monitored in both the positive and negative cables' shield-to-ground connections (sensors CH1 and CH2) during a healthy energization. Underdamped, though with less and more attenuated oscillations, was observed in the transient period in comparison with the simulations. These oscillations were rapidly dampened, and after current extinction at approximately 2 ms after energization, no significant currents were registered in the steady state. The current oscillations around zero in the steady state can be attributed to the rectifier, and the oscillating characteristic and settling to zero are indicators of successful energization.

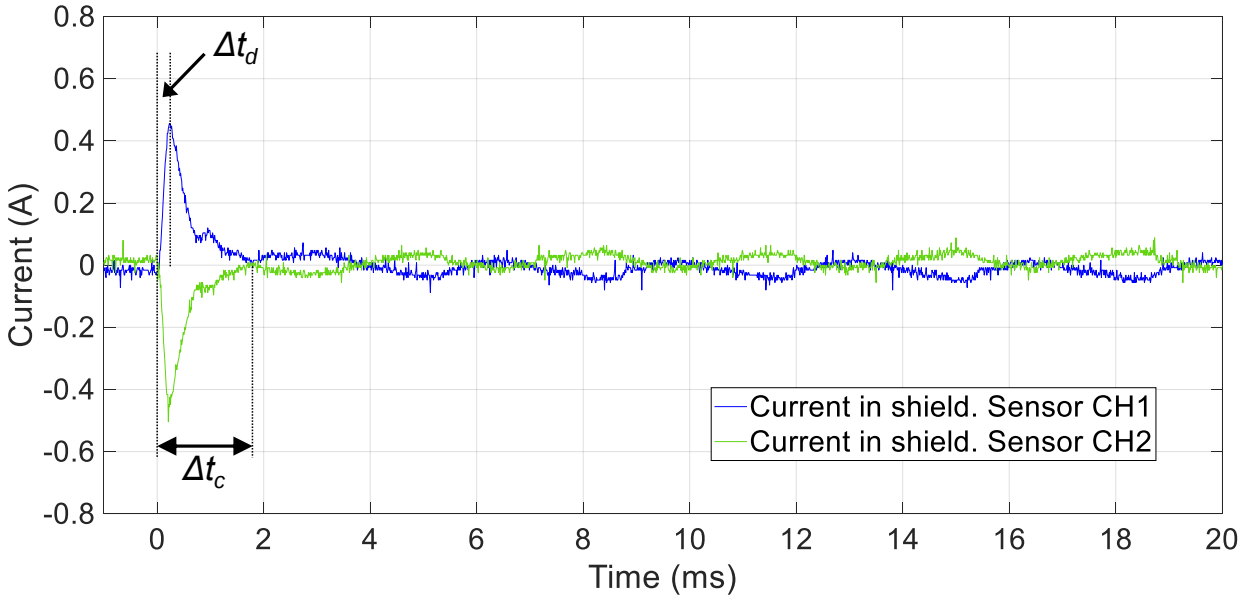

Figure 18. Experimental results. Shield currents for a healthy energization with a 100 Ω resistive load, V_{DC} = 50 V.

According to Figure 18, the shield currents dropped to zero approximately 2 ms after energization. This was the time corresponding to the first zero-crossing exhibited by these currents, at which threshold Δt_c should be set, according to Equation (15). On the other hand, for the derivative sign change criteria, Δt_d can be set at 0.18 ms, which is the first zero-crossing exhibited by the derivative (i.e., the first local minimum (negative pole measurement) or maximum (positive pole measurement)), as per Equation (18). As previously mentioned, it is apparent that the derivative sign change criterion allows for faster fault detection than the zero-crossing criterion ($\Delta t_d < \Delta t_c$). These experimental results are consistent with the principles described in Section 3 and the results obtained from the simulations, and were employed for fault detection in the following.

Moreover, from Figure 18, the fine-tuning of ε_c and ε_d can be performed based on the high-frequency noise in the shield current signal and the oscillations around zero during the steady-state conditions due to rectification. Specifically, ε_c can be set to the highest observed current spike in Figure 18 (ε_c = 85 mA), while ε_d can be established at the maximum slope exhibited during the oscillations (i.e., at the inflection points (ε_d = 50 A/s)).

It should be noted that the cable selection was carried out to closely match the characteristics of full-scale HVDC cables, with comparable RLC parameters per unit length to reflect the behavior of long HVDC cables. As no additional components such as resistors, inductors, or capacitors were used to compensate for the scaling of time constants, particularly those related to RC parameters, due to the difference in cable dimensions, the transient responses were found on a shorter time scale and therefore exhibited more attenuated oscillations compared to the simulated full-scale HVDC system. Despite

this difference, the shield currents displayed the same characteristic behaviors as those expected from a full-scale system. This consistency further validates the scaled-down experimental platform.

5.3. Faulty Energization Tests

Furthermore, various ground fault tests were conducted in the three cable sections, both between the positive and negative cables and shields. The shield currents on the rectifier side grounding connections were recorded, showing different transient waveforms. Different fault resistance (R_f) values were tested: 0, 1, 10, and 100 Ω. For example, as shown in Figure 19 (fault at B-B′, i.e., 100 m from the source in the positive cable) and Figure 20 (fault at Y-Y′, i.e., 100 m from the source in the negative cable), for a solid ground fault (R_f = 0 Ω), the shield current increased rapidly in the faulty pole with invariant polarity throughout the energization and subsequent time, without attaining any zero-crossing. When the currents reached steady-state operation, they settled in a DC component with the same corresponding polarity in the faulty pole shield. Because of the symmetry of the problem, opposite results were achieved for faults in the positive and negative poles, as seen in Figures 19 and 20. Therefore, by observing the current polarity or current derivative sign, the faulty cable can be easily identified.

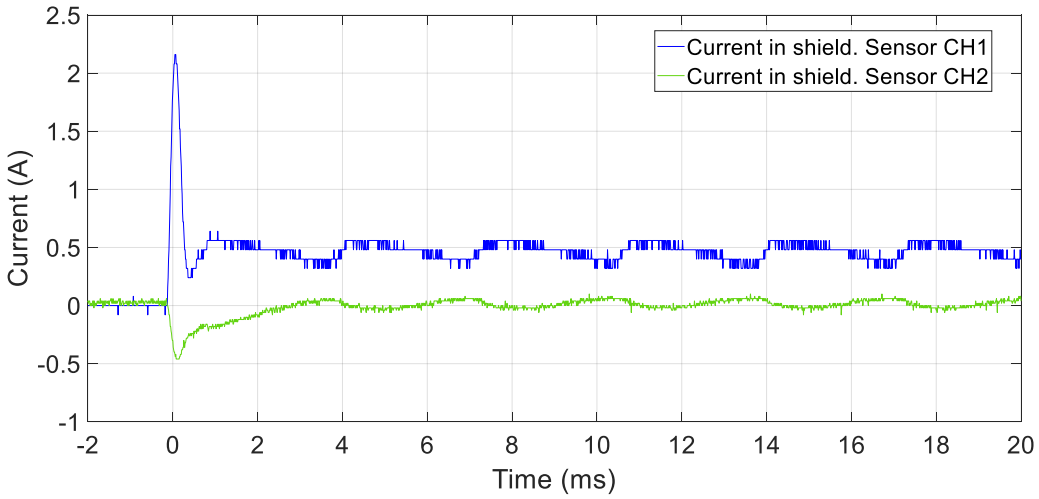

Figure 19. Experimental results. Shield currents for a faulty energization with a 100 Ω resistive load, V_{DC} = 50 V. Ground fault at B-B′ with R_f = 0 Ω.

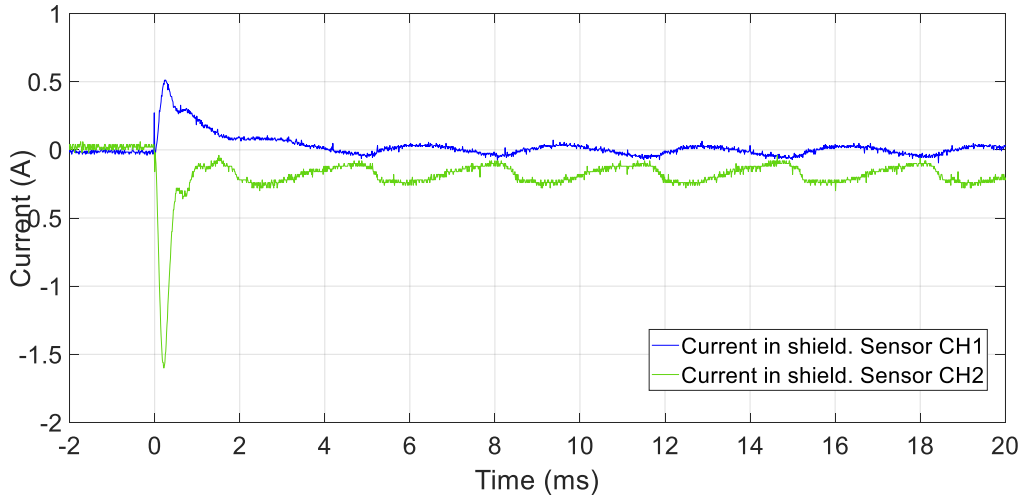

Figure 20. Experimental results. Shield currents for a faulty energization with a 100 Ω resistive load, V_{DC} = 50 V. Ground fault at Y-Y′ with R_f = 0 Ω.

Moreover, it is worth noting that, as per Figure 5 and Equation (14), the steady-state DC component of the shield current (K) depends on the applied voltage at the energization instant (V_{DC}) as well as on the system's resistive parameters (R_C and R_S). Therefore, in the experimental tests, the resulting DC component had a lower value compared to that in the full-scale HVDC cable simulations. However, despite this difference, the shield currents exhibited the same characteristic steady-state behavior, with $K \approx 0$ for healthy energizations and $K \neq 0$ faulty energizations. This consistency between the scaled-down experiment and the full-scale model further validates the reliability of the approach.

Table 3 shows some current features registered at the shield grounding connections during faulty energizations (peak current, I_{peak}, and DC steady-state current, I_{DC}) at ends A′ and X′ by sensors CH1 and CH2, respectively, for faults along both the positive and negative poles considering a 100 Ω resistive load, 50 V_{DC} voltage supply, and R_f = 0 Ω. As previously stated, ground faults in the positive or negative poles produce higher peaks during the energization of transient and DC components in the steady state in comparison with healthy energizations. These currents have the sign of the DC pole where the ground fault is located. However, fault location cannot be determined by current amplitudes, as they are dampened by the fault distance and resistance.

Table 3. Ground fault currents in the shield for different fault locations and zero fault resistance (R_f = 0).

Condition	Fault Location	Sensor CH1		Sensor CH2	
		I_{peak} [A]	I_{DC} [A]	I_{peak} [A]	I_{DC} [A]
Healthy	n/a	0.472	−0.011	−0.440	0.020
Faulty positive pole	A-A′	4.440	0.867	−0.720	0.025
	B-B′	2.160	0.449	−0.400	0.029
	C-C′	1.360	0.211	−0.416	0.009
Faulty negative pole	X-X′	0.720	−0.007	−4.080	−0.826
	Y-Y′	0.512	−0.005	−1.600	−0.456
	Z-Z′	0.480	−0.006	−2.040	−0.176

Figure 21 shows the measurement results captured in CH1 for faulty energizations with R_f values of 0 (solid short-circuit), 1, 10, and 100 Ω for ground faults at point B-B′. In the experimental tests, greater oscillations were observed with respect to the simulation results, this time obtaining an underdamped response in all faulty cases. It was verified that for lower R_f values, the damping effect on the shield current, the overshoot, and the steady-state DC component are greater.

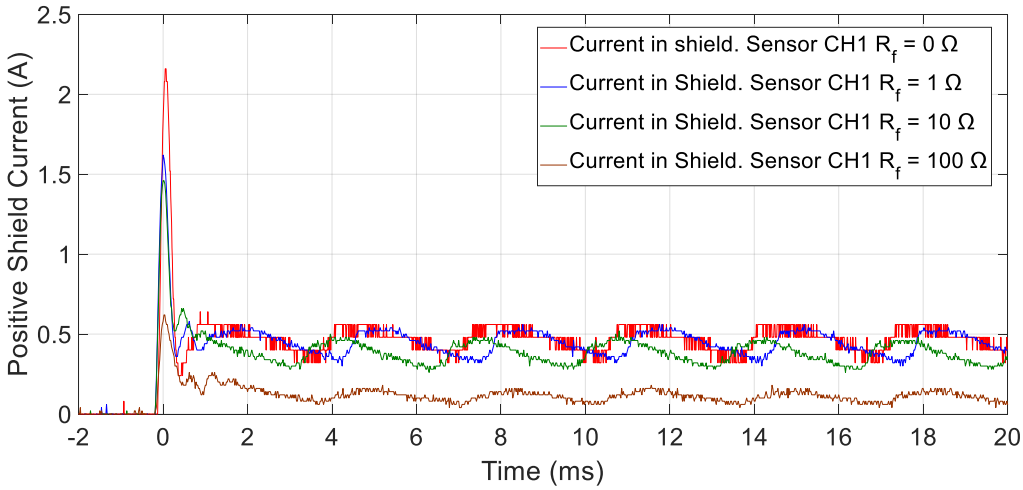

Figure 21. Experimental results. Shield currents in the positive pole for a faulty energization with a 100 Ω resistive load, V_{DC} = 50 V. Ground faults at B-B′ with fault resistances R_f = 0, 1, 10, and 100 Ω.

Additionally, the results show that during the faulty energizations, the shield current only had a positive sign throughout the process and subsequent time in all cases, settling to the corresponding constant DC value with the same polarity. Analogously, this current would have the opposite polarity if the fault was performed in the negative pole. Thus, no zero-crossing was attained in the shield current waveform, upholding the applicability of the zero-crossing criterion. Nevertheless, it can be derived that this fault detection criterion faces greater challenge for higher R_f values for which the captured values are not sufficiently high in order to trip reliably. Among the studied R_f values, R_f = 100 Ω was the most challenging, although it still implies shield current values considerably above zero that enable the fault detection through the zero-crossing criterion. On the other hand, the applicability of the derivative sign change criterion also presents a greater challenge for higher R_f values, as the lower damping effect may place the peak time close to the one under the healthy condition, requiring high-sensitivity measurement devices in order to capture the difference with respect to the threshold.

The shield current waveforms measured by sensor CH1 for healthy and faulty energizations are presented in Figure 22, with a time difference between energizations for clarity purposes. The faulty energization corresponds to the less severe, and therefore most challenging studied ground fault for both tripping criteria (R_f = 100 Ω), at the same fault location B-B′. According to Figure 22, the adjustment of the tripping threshold at its minimum operable value would imply Δt_c = 1.91 ms for the zero-crossing criterion stated in Equation (15). At the threshold time of Δt_c = 1.91 ms, the current is zero for the healthy energization and 165 mA for the faulty energization, complying with the tripping criteria established in Equation (16). For any delay above the threshold, the currents are sufficiently separated to enable proper fault detection. Similarly, the adjustment for the derivative sign change criterion stated in Equation (18) would imply Δt_d = 0.18 ms. At the threshold time of Δt_d = 0.18 ms, the current derivative was zero for the healthy energization, while it was significantly positive for the faulty energization, complying with the tripping criteria established in Equation (19).

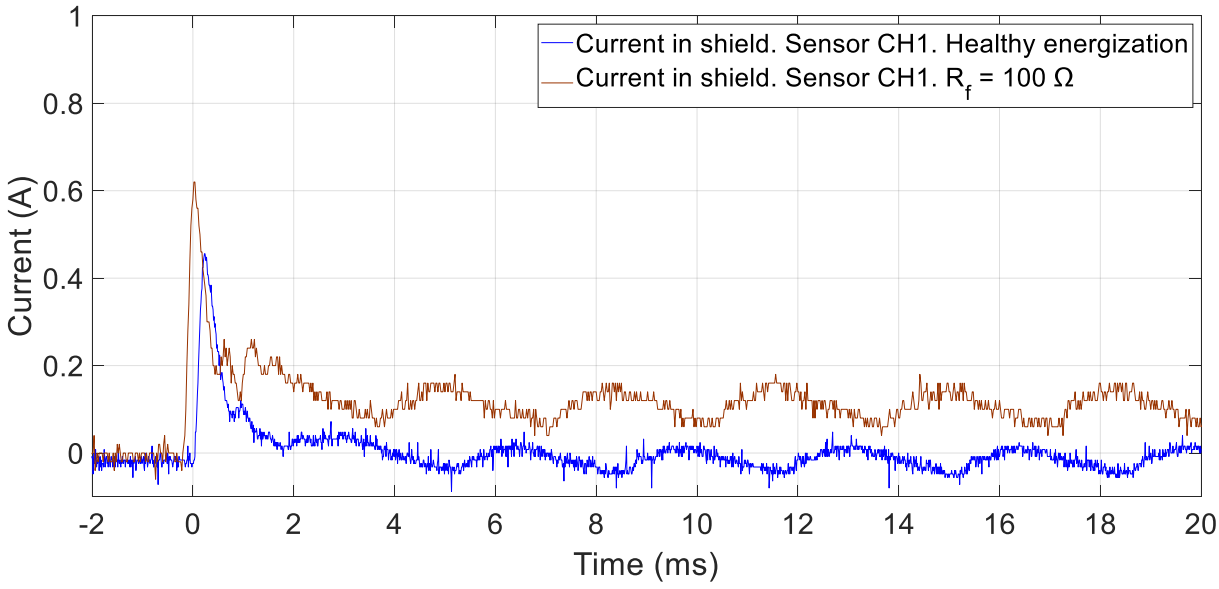

Figure 22. Experimental results. Shield currents for healthy and faulty energizations (ground fault at B-B′ with R_f = 100 Ω) with a 100 Ω resistive load, V_{DC} = 50 V.

The numerical application of the tripping criteria to the experimental results is presented in Table 4.

Table 4. Numeral application of the tripping criteria to the experimental results for a ground fault in the positive pole at B-B', with settings of Δt_c = 1.91 ms and Δt_d = 0.18 ms.

R_f [Ω]	I_{shield} [mA] at Δt_c	(16) Verified	dI_{shield}/dt [kA/s] at Δt_d	(19) Verified
0	510	Yes	−12.5	Yes
1	497		−9.1	
10	406		−8.2	
100	180		−3.4	

5.4. Discussion on the Selectivity and Sensitivity of the Proposed Method

5.4.1. Analysis of False Tripping Factors and Fine-Tuning

The experiments were carried out in a laboratory environment, accounting for several factors that could induce false tripping such as electromagnetic noise, harmonic distortion caused by the rectification with limited filtering, and measurement noise introduced by the current clamps used as sensors, as discussed in Section 3.3.

Each false tripping factor is hereby analyzed. The fine-tuning of the protection system is also described, which was performed according to the procedure described in Section 3.3 (i.e., by conducting an initial healthy energization to determine the optimal settings Δt_c and Δt_d, and finely adjusted thresholds ε_c and ε_d).

To assess the impact of electromagnetic noise on the shield current measurement, the time-domain current signal from the initial healthy energization was decomposed into its frequency components. The power spectral density and the value of the noise across the frequency spectrum were then computed, enabling an evaluation of the total deviation of the noise from zero.

Harmonic distortion due to limited filtering in the laboratory environment was evaluated by analyzing the harmonic content of the current during the initial healthy energization. The total harmonic distortion (THD) was quantified and related to the characteristic component of the shield current in order to determine its actual impact.

To investigate measurement noise introduced by the current clamps, the signal-to-noise ratio (SNR) was analyzed, as a low SNR can increase the probability of false tripping due to measurement noise. This analysis was conducted over various cable energizations, leading to the conclusion that the noise introduced by the measurement device could be modeled as zero-centered Gaussian noise.

Since the three noise sources—electromagnetic, harmonic and measurement—are independent, they were combined quadratically to set a conservative threshold. The total fluctuation was set at three times the combined mean noise value: ε_c = 85 mA (16.90% of the peak value during a healthy energization). On the other hand, ε_d was simply tuned by analyzing the maximum error in the derivative calculations obtained from constant shield current tests, yielding a value of ε_d = 50 A/s. These threshold values represent the critical current and current-derivative that could lead to false tripping due to the cumulative effect of the mentioned factors.

5.4.2. Selectivity Assessment

The selectivity of the proposed method, defined as its ability to distinguish between faulty energizations and normal system transients including those from healthy energizations is reinforced by the conservative threshold settings, which account for the various noise sources (electromagnetic, harmonic, and measurement noise).

The noise assessment integrates the contributions from all noise sources to ensure that the system is robust against fluctuations. The established thresholds ensure that no false tripping occurs during healthy energizations, as the noise-induced current is below the limits. The margin between the noise levels and the current threshold provides a safe buffer, preventing unnecessary trips during normal operations.

The results demonstrate the system's capability to discriminate between healthy and faulty energizations. The zero-crossing criterion provided a selectivity factor of 6000 for

solid faults, meaning that the fault-induced current was 6000 times larger than the noise-induced fluctuations. Even in the case of high-resistance faults, the selectivity remained robust, with a ratio of 2.25 between the fault current and the detection threshold. This ensured that the system remained highly selective, minimizing the risk of false tripping during normal energizations.

For the derivative sign change criterion, the system exhibited a selectivity ratio of 250 for solid faults and 68 for high-resistance faults. This criterion outperformed the zero-crossing criterion for higher fault resistance values. The fault-induced derivative of the shield current significantly exceeded the noise-induced derivative fluctuations, allowing the system to quickly and accurately distinguish between transient faults and normal operating conditions.

5.4.3. Sensitivity Assessment

The results indicate the high sensitivity of the proposed method, defined as its ability to detect even less severe faulty energizations, particularly those with ground faults with high fault resistance. This sensitivity was achieved by setting the thresholds based on the detailed noise analysis, allowing the system to detect low-magnitude fault currents without being influenced by noise.

For instance, the experimental results showed that the system could reliably detect faults with resistance values as high as $R_f = 100\ \Omega$. The calculated ratio between the measured shield current and the threshold for these high-resistance faults was 2.25, indicating that even in the worst-case scenario (highest fault resistance), the fault current remained significantly above the detection threshold. This ensures that the protection method retains high sensitivity to ground faults, even when the fault current is heavily attenuated by fault resistance.

Furthermore, the ratio between the actual fault current derivative and the threshold ranged from 250 for solid faults to 68 for high-resistance faults. This further underscores the system's sensitivity to faulty energizations, ensuring that even subtle variations in the shield current derivative, such as those caused by high-resistance faults, are reliably detected.

5.5. General Discussion

The experimental results strongly uphold the research on the zero-crossing method, while the shield current remains non-negligible with the same polarity as well as the derivative sign change setting method, so the shield current presents a sufficiently large derivative when the threshold time is attained. Larger-scale experimental tests are necessary to thoroughly analyze the derivative sign change setting method, as the method can be compromised if ground faults with high fault resistance can approach a peak time similar to the one corresponding to healthy conditions. Due to computation and resolution requirements, especially for higher fault resistance energizations (R_f values significantly above 100 Ω), the implementation of the derivative change sign setting option in small-scale DC laboratory setups needs appropriate devices with high-resolution data acquisition.

Evidently, in the case of a ground fault at Y-Y', the results would be analogous with opposite polarity, applying Equations (17) and (20). Furthermore, it was again verified that according to the shield grounding connection for which these conditions are satisfied (positive or negative), the faulty pole can be easily identified as opposed to the fault location, which is hampered by the dependence on the fault distance and resistance.

The results obtained from the experimental tests are consistent with the simulation results, despite the differences in transient behavior due to the differences in RLC parameters, which resulted in different time constants, leading to different damping effects on the responses to energization. Moreover, it has been demonstrated that the theoretical and operational principles of the proposed method extend their applicability to the different possible transient behaviors.

The threshold settings according to the healthy energization characteristic and the application of the protection method to faulty energizations were carried out at experimental LV without significant differences. Both criteria were verified, confirming that the derivative sign change criterion allows for faster fault detection to the detriment of reliability for higher fault resistances, while the other way around, the zero-crossing criterion ensures reliability for higher fault resistance at the expense of fault detection time.

The non-suitability of di/dt protective relaying to detect faulty energizations with high R_f ground faults was equally derived from the experimental results, as notable differences were not observed between the derivative behavior of inrush currents and that of ground faults. Similarly, the non-suitability of i> was also sustained by the experimental results, as the magnitude of inrush currents has been demonstrated to be close to that of fault currents in certain cases. By implementing correct protection coordination by setting a time delay or the blocking of di/dt and i> relaying functions during energization, unwanted trips during healthy energizations can be avoided, and protection against faulty energizations, even for high R_f ground faults, can be ensured through the proposed method.

6. Conclusions

This paper proposes a novel method for distinguishing between the healthy and faulty energizations of HVDC cables, based on the real-time monitoring of the currents at the grounding terminals of the cable shield. This approach avoids mismatches in protection systems and false tripping. Moreover, this method eliminates the need for the trip blocking delays typically required in conventional ground fault protections, enabling earlier and more reliable tripping and fault clearing, thus reducing potential damage to the cable and the converter.

During both healthy and faulty energizations, transient leakage currents circulate through the HVDC cable shields, but their transient behaviors differ substantially. These differences were leveraged to develop the proposed method. The method involves setting the tripping time to the zero-crossing of the shield current waveform for a healthy energization. If the current remains non-zero after this time, it implies the presence of a ground fault, prompting the relays to initiate the tripping sequence. Alternatively, the tripping time can be set according to the current's first derivative sign change, allowing for faster tripping at the cost of reliability for high-resistance ground faults. Fine-tuning the protection system parameters requires an initial healthy energization performed during the protection commissioning phase.

The protection method was verified through extensive computer simulations and experimental tests, yielding satisfactory and consistent results with fair response times, defined as the minimum time period during which the current waveform is expected to oscillate sufficiently to detect the fault.

A major advantage of this technique is that it eliminates the need for HV devices by measuring currents in the cable shields, thereby remarkably reducing the investment costs. This method can improve HVDC line protection through proper coordination, overcoming the limitations of conventional methods during energizations, especially for high fault resistance ground faults. Otherwise, the lack of selectivity of these protections can lead to destructive consequences for HVDC equipment in the event of faulty energizations.

Future work may extend this study to precise fault location. While the proposed method can effectively identify the faulty cable, it does not pinpoint the exact fault location. Additionally, larger-scale tests should be conducted on HVDC transmission cables to obtain more representative results by aligning the electrical parameters—and therefore the transient behaviors—to those of real-scale HVDC lines. With further testing in larger-scale systems, more precise evaluations of the method's performance including selectivity and sensitivity could be achieved.

Author Contributions: Conceptualization, K.M. and R.G.; Methodology, K.M., J.M.G. and R.G.; Software, K.M. and R.G.; Validation, K.M., J.M.G. and C.A.P.; Formal analysis, K.M. and J.M.G.; Investigation, K.M. and J.M.G.; Resources, C.A.P.; Data curation, R.G. and J.M.G.; Writing—original draft preparation, K.M., R.G. and J.M.G.; Writing—review and editing, K.M. and J.M.G.; Visualization, K.M. and J.M.G.; Supervision, R.G. and C.A.P.; Project administration, R.G. and C.A.P.; Funding acquisition, C.A.P. All authors have read and agreed to the published version of the manuscript.

Funding: This research received no external funding.

Data Availability Statement: Datasets are available on request from the authors.

Conflicts of Interest: The authors declare no conflicts of interest.

References

1. Wang, M.; Li, W.; Wang, S.; Xu, Q.; Zhang, X. Review and Outlook of HVDC Grids as Backbone of Transmission System. *CSEE J. Power Energy Syst.* **2021**, *7*, 797–810. [CrossRef]
2. MacLeod, N.; Jusan Cattan, F. *High Voltage DC Transmission Systems*; Planning Studies for an HVDC Project; Springer: Cham, Switzerland, 2024; pp. 1–38, ISBN 978-3-030-71619-6.
3. Fang, Y.; Liu, Y.; Fu, A.; Shi, S.; Zhang, Z. A Data-Driven Control for Modular Multilevel Converters Based on Model-Free Adaptive Control with an Event-Triggered Scheme. *Electronics* **2024**, *13*, 2899. [CrossRef]
4. Zhao, Q.; García-González, J.; García-Cerrada, A.; Renedo, J.; Rouco, L. *Transmission Expansion Planning: The Network Challenges of the Energy Transition*; HVDC in the Future Power Systems; Springer: Cham, Switzerland, 2021; pp. 117–151, ISBN 978-3-030-49428-5.
5. Dambone Sessa, S.; Chiarelli, A.; Benato, R. Availability Analysis of HVDC-VSC Systems: A Review. *Energies* **2019**, *12*, 2703. [CrossRef]
6. Kalair, A.; Abas, N.; Khan, N. Comparative Study of HVAC and HVDC Transmission Systems. *Renew. Sustain. Energy Rev.* **2016**, *59*, 1653–1675. [CrossRef]
7. Luo, Y.; Liu, C.; He, Z.; Jiang, Y.; Chen, Q. Power Flow Calculation for AC/DC Power Systems with Line-Commutated Converter–Modular Multilevel Converter (LCC-MMC) Hybrid High-Voltage Direct Current (HVDC) Based on the Holomorphic Embedding Method. *Electronics* **2024**, *13*, 1877. [CrossRef]
8. Chen, L.; Zhang, W.; Liu, B.; Wang, L.; Li, Y. Performance Evaluation Approach of Superconducting Fault Current Limiter in MMC-HVDC Transmission System. *IEEE Trans. Appl. Supercond.* **2021**, *31*, 5602507. [CrossRef]
9. Van Hertem, D.; Gollan, S.; Jovcic, D.; Callavik, M.; Eriksson, M. Substations for Future HVdc Grids: Equipment and Configurations for Connection of HVdc Network Elements. *IEEE Power Energy Mag.* **2019**, *17*, 56–66. [CrossRef]
10. Singh, N.K.; Carlsson, J.X. Energization Study of Five-Terminal Multi-Level HVDC Converter Station. In Proceedings of the 2013 IEEE Power & Energy Society General Meeting, Vancouver, BC, Canada, 21–25 July 2013; pp. 1–5. [CrossRef]
11. Li, Y.; Shi, X.; Liu, B.; Lei, W.; Wang, F.; Tolbert, L.M. Development, Demonstration, and Control of a Testbed for Multiterminal HVDC System. *IEEE Trans. Power Electron.* **2017**, *32*, 6069–6078. [CrossRef]
12. Wang, P.; Zhang, X.-P.; Coventry, P.F.; Zhang, R. Start-Up Control of an Offshore Integrated MMC Multi-Terminal HVDC System with Reduced DC Voltage. *IEEE Trans. Power Syst.* **2016**, *31*, 2740–2751. [CrossRef]
13. Radwan, M.; Azad, S.P. Protection of Multi-Terminal HVDC Grids: A Comprehensive Review. *Energies* **2022**, *15*, 9552. [CrossRef]
14. Bucher, M.K.; Franck, C.M. Contribution of Fault Current Sources in Multiterminal HVDC Cable Networks. *IEEE Trans. Power Deliv.* **2013**, *28*, 1796–1803. [CrossRef]
15. Bucher, M.K. Transient Fault Currents in HVDC VSC Networks During Pole-to-Ground Faults. Ph.D. Thesis, ETH Zurich, Zurich, Switzerland, 2014. Available online: https://www.research-collection.ethz.ch/handle/20.500.11850/98128 (accessed on 13 September 2024).
16. Bucher, M.K.; Franck, C.M. Analytic Approximation of Fault Current Contributions from Capacitive Components in HVDC Cable Networks. *IEEE Trans. Power Deliv.* **2015**, *30*, 74–81. [CrossRef]
17. Bucher, M.K.; Franck, C.M. Analytic Approximation of Fault Current Contributions from AC Networks to MTDC Networks During Pole-to-Ground Faults. *IEEE Trans. Power Deliv.* **2016**, *31*, 20–27. [CrossRef]
18. Granizo, R.; Platero, C.A.; Guerrero, J.M. HVDC Ground Fault Detection Method Based on the Shield Leakage Current Measurement for Long Cable Energization. In Proceedings of the 2020 IEEE International Conference on Environment and Electrical Engineering and 2020 IEEE Industrial and Commercial Power Systems Europe (EEEIC/I&CPS Europe), Madrid, Spain, 9–12 June 2020; pp. 1–5. [CrossRef]
19. Zhang, L.; Tai, N.; Huang, W.; Liu, J.; Li, Y. A Review on Protection of DC Microgrids. *J. Mod. Power Syst. Clean Energy* **2018**, *6*, 1113–1127. [CrossRef]
20. Dave, J.; Ergun, H.; Van Hertem, D. Incorporating DC Grid Protection, Frequency Stability, and Reliability into Offshore DC Grid Planning. *IEEE Trans. Power Deliv.* **2020**, *35*, 2772–2781. [CrossRef]

21. Wang, Z.; Shi, X.; Tolbert, L.M.; Wang, F.; Blalock, B.J. A di/dt Feedback-Based Active Gate Driver for Smart Switching and Fast Overcurrent Protection of IGBT Modules. *IEEE Trans. Power Electron.* **2014**, *29*, 3720–3732. [CrossRef]
22. Huang, X.; Qi, L.; Pan, J. A New Protection Scheme for MMC-Based MVDC Distribution Systems with Complete Converter Fault Current Handling Capability. *IEEE Trans. Ind. Appl.* **2019**, *55*, 4515–4523. [CrossRef]
23. Shao, W.; Lin, J.; Zhang, J.; Sun, H.; Wu, X. A Power Module for Grid Inverter with In-Built Short-Circuit Fault Current Capability. *IEEE Trans. Power Electron.* **2020**, *35*, 10567–10579. [CrossRef]
24. Benadja, M.; Rezkallah, M.; Benhalima, S.; Hamadi, A.; Chandra, A. Hardware Testing of Sliding Mode Controller for Improved Performance of VSC-HVDC Based Offshore Wind Farm Under DC Fault. *IEEE Trans. Ind. Appl.* **2019**, *55*, 2053–2063. [CrossRef]
25. Nguyen, T.H.; Lee, D.-C. A Novel Submodule Topology of MMC for Blocking DC-Fault Currents in HVDC Transmission Systems. In Proceedings of the 2015 9th International Conference on Power Electronics and ECCE Asia (ICPE-ECCE Asia), Seoul, Republic of Korea, 1–5 June 2015; pp. 2057–2063. [CrossRef]
26. Wang, L.; Lin, C.; Wu, H.; Prokhorov, A.V. Stability Analysis of a Microgrid System with a Hybrid Offshore Wind and Ocean Energy Farm Fed to a Power Grid Through an HVDC Link. *IEEE Trans. Ind. Appl.* **2018**, *54*, 2012–2022. [CrossRef]
27. Chang, B.; Cwikowski, O.; Barnes, M.; Shuttleworth, R.; Beddard, A.; Coventry, P. Review of Different Fault Detection Methods and Their Impact on Pre-Emptive VSC-HVDC DC Protection Performance. *High Voltage* **2017**, *2*, 211–219. [CrossRef]
28. Haileselassie, T. Control, Dynamics and Operation of Multi-Terminal VSC-HVDC Transmission Systems. Ph.D. Thesis, NTNU, Trondheim, Norway, 2012. Available online: https://ntnuopen.ntnu.no/ntnu-xmlui/handle/11250/257409 (accessed on 13 September 2024).
29. Pragati, A.; Mishra, M.; Rout, P.K.; Gadanayak, D.A.; Hasan, S.; Prusty, B.R. A Comprehensive Survey of HVDC Protection System: Fault Analysis, Methodology, Issues, Challenges, and Future Perspective. *Energies* **2023**, *16*, 4413. [CrossRef]
30. Muniappan, M. A Comprehensive Review of DC Fault Protection Methods in HVDC Transmission Systems. *Prot. Control Mod. Power Syst.* **2021**, *6*, 1. [CrossRef]
31. Sahebkar Farkhani, J.; Çelik, Ö.; Ma, K.; Bak, C.L.; Chen, Z. A Comprehensive Review of Potential Protection Methods for VSC Multi-Terminal HVDC Systems. *Renew. Sustain. Energy Rev.* **2024**, *192*, 114280. [CrossRef]
32. Pérez-Molina, M.J.; Larruskain, D.M.; Eguía López, P.; Buigues, G.; Valverde, V. Review of Protection Systems for Multi-Terminal High Voltage Direct Current Grids. *Renew. Sustain. Energy Rev.* **2021**, *144*, 111037. [CrossRef]
33. Song, G.; Cai, X.; Li, D.; Gao, S.; Suonan, J. A Novel Pilot Protection Principle for VSC-HVDC Cable Lines Based on Fault Component Current. In Proceedings of the 2012 Power Engineering and Automation Conference, Wuhan, China, 18–20 September 2012; pp. 1–4. [CrossRef]
34. Lenz, M.; Oprea, L.; Popescu, V.; Hibberts-Casw, R. Analysis of Fault Location Methods for HVDC Transmission Systems Using Overhead Lines and Cables. In Proceedings of the VDE High Voltage Technology 2020, ETG-Symposium, Online, 9–11 November 2020; pp. 1–6.
35. Haleem, N.M.; Rajapakse, A.D. Fault-Type Discrimination in HVDC Transmission Lines Using Rate of Change of Local Currents. *IEEE Trans. Power Deliv.* **2020**, *35*, 117–129. [CrossRef]
36. Sneath, J.; Rajapakse, A.D. Fault Detection and Interruption in an Earthed HVDC Grid Using ROCOV and Hybrid DC Breakers. *IEEE Trans. Power Deliv.* **2016**, *31*, 973–981. [CrossRef]
37. Fletcher, S.; Norman, P.; Galloway, S.; Burt, G. Fault Detection and Location in DC Systems from Initial di/dt Measurement. In Proceedings of the Euro Tech Con Conference, Manchester, UK, 1 September 2003; pp. 1–15.
38. Haleem, N.M.; Rajapakse, A.D. Local Measurement Based Ultra-Fast Directional ROCOV Scheme for Protecting Bi-Pole HVDC Grids with a Metallic Return Conductor. *Int. J. Electr. Power Energy Syst.* **2018**, *98*, 323–330. [CrossRef]
39. Yousaf, M.Z.; Liu, H.; Raza, A.; Baig, M.B. Primary and Backup Fault Detection Techniques for Multi-Terminal HVDC Systems: A Review. *IET Gener. Transm. Distrib.* **2020**, *14*, 5261–5276. [CrossRef]
40. Ashrafi Niaki, S.H.; Hosseini, S.M.; Abdoos, A.A. Fault Detection of HVDC Cable in Multi-Terminal Offshore Wind Farms Using Transient Sheath Voltage. *IET Renew. Power Gener.* **2017**, *11*, 1707–1713. [CrossRef]
41. Ashrafi Niaki, S.H.; Karegar, H.; Ghalei, M. A Novel Fault Detection Method for VSC-HVDC Transmission System of Offshore Wind Farm. *Int. J. Electr. Power Energy Syst.* **2015**, *73*, 475–483. [CrossRef]
42. Granizo Arrabé, R.; Platero, C.A.; Álvarez Gómez, F.; Rebollo López, E. New Differential Protection Method for Multiterminal HVDC Cable Networks. *Energies* **2018**, *11*, 3387. [CrossRef]
43. Granizo, R.; Guerrero, J.M.; Álvarez, F.; Platero, C.A. Ground Fault Directional Protection Method for HVDC Multiterminal Networks. *IEEE Trans. Ind. Appl.* **2022**, *58*, 1573–1580. [CrossRef]
44. Ametani, A.; Nagaoka, N.; Baba, Y.; Ohno, T.; Yamabuki, K. *Power System Transients: Theory and Applications*, 2nd ed.; CRC Press: Boca Raton, FL, USA, 2016; ISBN 978-149-878-237-1.
45. *IEC TR 60919-2:2008*; Performance of High-Voltage Direct Current (HVDC) Systems with Line-Commutated Converters—Part 2: Faults and Switching. International Electrotechnical Commission (IEC): Geneva, Switzerland, 2008.

46. Høidalen, H.K. ATPDraw: The Graphical Preprocessor to ATP Electromagnetic Transients Program. Available online: https://www.atpdraw.net (accessed on 13 September 2024).
47. Gustavsen, B.; Semlyen, A. Rational Approximation of Frequency Domain Responses by Vector Fitting. *IEEE Trans. Power Deliv.* **1999**, *14*, 1052–1061. [CrossRef]